Seeing in the dark – II. Cosmic shear in the Sloan Digital Sky Survey

Eric M. Huff[1], Tim Eifler[2], Christopher M. Hirata[3], Rachel Mandelbaum[4,5], David Schlegel[6], Uroš Seljak[6,7,8,9]

[1] *Department of Astronomy, University of California at Berkeley, Berkeley, CA 94720, USA*
[2] *Center for Cosmology and Astro-Particle Physics, The Ohio State University, 191 W. Woodruff Avenue, Columbus, OH 43210, USA*
[3] *Department of Astronomy, Caltech M/C 350-17, Pasadena, CA 91125, USA*
[4] *Department of Astrophysical Sciences, Princeton University, Peyton Hall, Princeton, NJ 08544, USA*
[5] *Department of Physics, Carnegie Mellon University, Pittsburgh, PA 15213, USA*
[6] *Lawrence Berkeley National Laboratory, Berkeley, CA 94720, USA*
[7] *Space Sciences Lab, Department of Physics and Department of Astronomy, University of California, Berkeley, CA 94720, USA*
[8] *Institute of the Early Universe, Ewha Womans University, Seoul, Korea*
[9] *Institute for Theoretical Physics, University of Zurich, Zurich, Switzerland*

15 December 2011

ABSTRACT

Statistical weak lensing by large-scale structure – cosmic shear – is a promising cosmological tool, which has motivated the design of several large upcoming surveys. Here, we present a measurement of cosmic shear using coadded Sloan Digital Sky Survey (SDSS) imaging in 168 square degrees of the equatorial region, with $r < 23.5$ and $i < 22.5$, a source number density of 2.2 per arcmin^2 and median redshift of $z_{\mathrm{med}} = 0.52$. These coadds were generated using a new method described in the companion Paper I (Huff et al. 2011) that was intended to minimise systematic errors in the lensing measurement due to coherent PSF anisotropies that are otherwise prevalent in the SDSS imaging data. We present measurements of cosmic shear out to angular separations of 2 degrees, along with systematics tests that (combined with those from Paper I on the catalogue generation) demonstrate that our results are dominated by statistical rather than systematic errors. Assuming a cosmological model corresponding to WMAP7 (Komatsu et al. 2011) and allowing only the amplitude of matter fluctuations σ_8 to vary, we find a best-fit value of $\sigma_8 = 0.636^{+0.109}_{-0.154}$ (1σ); without systematic errors this would be $\sigma_8 = 0.636^{+0.099}_{-0.137}$ (1σ). Assuming a flat ΛCDM model, the combined constraints with WMAP7 are $\sigma_8 = 0.784^{+0.028}_{-0.026}(1\sigma)^{+0.055}_{-0.054}(2\sigma)$ and $\Omega_m h^2 = 0.1303^{+0.0047}_{-0.0048}(1\sigma)^{+0.009}_{-0.009}(2\sigma)$; the 2σ error ranges are respectively 14 and 17 per cent smaller than WMAP7 alone. Aside from the intrinsic value of such cosmological constraints from the growth of structure, we identify some important lessons for upcoming surveys that may face similar issues when combining multi-epoch data to measure cosmic shear.

Key words: cosmology: observations – gravitational lensing: weak – surveys.

1 INTRODUCTION

As a result of gravitational lensing, large scale inhomogeneities in the matter density field produce small but systematic fluctuations in the sizes, shapes, and fluxes of distant objects that are coherent across large scales. This effect was first suggested as a tool for constraining the form of the metric in 1966 by Kristian & Sachs (1966). In a more modern context, the two-point statistics of lensing fluctuations allow the only truly direct measurement of the matter power spectrum and the growth of structure at late times, when

dark energy has caused an accelerated expansion of the universe (Riess et al. 1998; Perlmutter et al. 1999) and affected the growth of structure. Many studies have pointed out that high signal-to-noise cosmic shear measurements would be extraordinarily sensitive probes of cosmological parameters (e.g., Huterer 1998; Benabed & van Waerbeke 2004), which led to its being flagged as one of the most promising probes of dark energy by the Dark Energy Task Force (Albrecht et al. 2006). Direct measurements of the growth of structure also offer the opportunity to test alternative models of gravity (e.g., Laszlo et al. 2011).

Cosmic shear measurements were attempted as early as 1967 (Kristian 1967), but until the turn of the millennium (Bacon et al. 2000; Kaiser et al. 2000; van Waerbeke et al. 2000; Wittman et al. 2000), no astronomical survey had the statistical power to detect it. The difficulty of the measurement is a consequence of the near-homogeneity and isotropy of the universe. An order unity distortion to galaxy images requires an integrated line-of-sight matter over-density of:

$$\Sigma_{\mathrm{crit}} = \frac{c^2}{4\pi G} \frac{d_S}{d_L \, d_{LS}} \tag{1}$$

where d_S, d_L, and d_{LS} are the angular diameter distances from the observer to the background source, from the observer to the lens, and from the lens to the background source, respectively. A fluctuation in the surface density $\Delta\Sigma$ leads to a shear distortion $\gamma \sim \Delta\Sigma/\Sigma_{\mathrm{crit}}$.

Averaged over large (~ 100 Mpc) scales, typical line-of-sight matter fluctuations are only $10^{-3}\Sigma_{\mathrm{crit}}$. The primary source of noise in the shear measurement, the random intrinsic dispersion in galaxy shapes, is orders of magnitude larger; typically the shape noise results in a dispersion in the shear of $\sigma_\gamma = 0.2$. Worse, even in modern ground-based astronomical imaging surveys, the coherent distortions – or point-spread function (PSF) – induced by effects of the atmosphere, telescope optics, and detectors are typically several times larger than the cosmological signal (e.g., Heymans et al. 2011 and Paper I in this series). Estimating the distances to the background sources is both crucial (Ma et al. 2006) and difficult (Ma & Bernstein 2008; Bernstein & Huterer 2010); errors there will modulate the amplitude of the signal through Σ_{crit}, biasing inference of the growth of structure.

These obstacles define the observational problem. While the existence of cosmic shear has been established by the first studies to detect the effect, the full potential of cosmological lensing remains to be exploited. Few data sets capable of achieving the signal strength for a cosmologically competitive measurement presently exist – the Canada-France-Hawaii Telescope Legacy Survey (CFHTLS; Hoekstra et al. 2006; Semboloni et al. 2006; Benjamin et al. 2007; Fu et al. 2008), the Cosmological Evolution Survey (COSMOS; Massey et al. 2007a; Schrabback et al. 2010), and the subset of the SDSS imaging studied here. However, several large surveys are planned for the immediate and longer-term future that will substantially expand the amount of available data for cosmological weak lensing studies. In the next few years, these include Hyper Suprime-Cam (HSC, Miyazaki et al. 2006), Dark Energy Survey (DES[1], The Dark Energy Survey Collaboration 2005), the KIlo-Degree Survey (KIDS[2]), and the Panoramic Survey Telescope and Rapid Response System (Pan-STARRS[3], Kaiser et al. 2010). Further in the future, there are even more ambitious programs such as the Large Synoptic Survey Telescope (LSST[4], LSST Science Collaborations et al.

2009), Euclid[5], and the Wide-Field Infrared Survey Telescope (WFIRST[6]).

For this work, we have combined several methods discussed in the literature as viable techniques for measuring cosmic shear while removing common systematic errors. In Paper I (Huff et al. 2011), we began with the PSF model generated by the Sloan Digital Sky Survey (SDSS) pipeline over ~ 250 deg^2 that had been imaged many times, and employed a rounding kernel method similar to that proposed in Bernstein & Jarvis (2002). The result, after appropriate masking of problematic regions, was 168 square degrees of deep coadded imaging with a well controlled, homogeneous PSF and sufficient galaxy surface density to measure a cosmic shear signal. The usable area in r band was only 140 square degrees because of a PSF model error problem on the camcol 2 charge-coupled device (CCD), which is suspected to be an amplifier non-linearity problem.

In this work, we use the catalogue from Paper I to produce a cosmic shear measurement that is dominated by statistical errors. Section 3 enumerates the primary sources of systematic error when measuring cosmic shear using our catalogue (the properties of which are summarized briefly in Sec. 2), and describes our approaches to constraining each of them. In Section 4, we outline our correlation function estimator and several transformations of it that are used for systematics tests. Our methods for estimating covariance matrices for our observable quantities (both due to statistical and systematic errors) are described in Sec. 5. Finally, section 6 presents the constraining power of this measurement alone for a fiducial cosmology, and in combination with the 7-year *Wilkinson Microwave Anisotropy Probe* (WMAP7, Komatsu et al. 2011) parameter constraints to produce a posterior probability distribution over $\Omega_m h^2$, $\Omega_b h^2$, σ_8, n_s, and w. We show that in addition to its value as an independent measurement of the late-time matter power spectrum, this measurement provides some additional constraining power over WMAP7 within the context of ΛCDM. We conclude with some lessons for the future in Sec. 7.

While this work was underway, we learned of a parallel effort by Lin et al. (2011). These two efforts use different methods of coaddition, different shape measurement codes, different sets of cuts for the selection of input images and galaxies, and analyze their final results in different ways; what they have in common is their use of SDSS data (not necessarily the same sets of input imaging) and their use of the SDSS PHOTO pipeline for the initial reduction of the single epoch data and the final reduction of the coadded data (however, they use different versions of PHOTO). Using these different methods, both groups have extracted the cosmic shear signal and its cosmological interpretations. We have coordinated submission with them but have not consulted their results prior to this, so these two analysis efforts are independent, representing versions of two independent pipelines.

---

[1] https://www.darkenergysurvey.org/
[2] http://www.astro-wise.org/projects/KIDS/
[3] http://pan-starrs.ifa.hawaii.edu/public/
[4] http://www.lsst.org/lsst

[5] http://sci.esa.int/science-e/www/area/index.cfm?fareaid=102
[6] http://wfirst.gsfc.nasa.gov/

2 CATALOGUES

Paper I (Huff et al. 2011) describes a coadd imaging dataset, optimised for cosmic shear measurement, constructed from single-epoch SDSS images in the Stripe 82 equatorial region, with right ascension (RA) $-50° <$RA$< +45°$, and declination $-1.25° <$Dec$< +1.25°$. In that work, we apply an adaptive rounding kernel to the single-epoch images to null the effects of PSF anisotropy and match to a single homogeneous PSF model for the entire region, and show that in the resulting shear catalogues, the amplitude of the galaxy shape correlations due to PSF anisotropy at angular separations greater than 1 arcminute is negligible compared to the expected cosmic shear statistical errors.

The final shape catalogue described in that work consists of 1 067 031 r-band and 1 251 285 i-band shape measurements with characteristic limiting magnitudes of $r < 23.5$ and $i < 22.5$, over effective areas of 140 and 168 square degrees, respectively.

3 MODEL FOR THE LENSING AND SYSTEMATIC ERROR SIGNALS

We model the observed galaxy shape field as the sum of a cosmic shear component, an independent systematics field produced by anisotropies in the effective PSF e_{psf}, and a systematics field produced by the intrinsic spatial correlations of galaxy shapes e_{int} (intrinsic alignments; e.g., Hirata & Seljak 2004). We allow for a shear calibration factor that depends on the shear responsivity $\mathcal{R}$ (Bernstein & Jarvis 2002) of the ensemble of galaxy surface brightness profiles to the underlying gravitationally-induced shear γ. Typically $\mathcal{R} \approx 1 - e_{rms}^2$, however we consider it to be a more general factor that also includes any biases due to effects such as uncorrected PSF dilution, noise-related biases, or selection biases. We assume that the galaxy shape response to PSF anisotropies $\mathcal{R}_{psf}$ is not *a priori* known, but rather suffers from a similar set of 'calibration' uncertainties as the response of the ensemble of galaxy images to gravitational lensing shear. Thus we define our model for the two ellipticity components $e = (e_1, e_2)$ as

$$e = \mathcal{R}\gamma + \mathcal{R}_{psf}e_{psf} + e_{int}. \tag{2}$$

We assume that the two-point statistics of the underlying (cosmological) shear field $\langle \gamma\gamma \rangle$ consist entirely of E-modes, $e_{\gamma,E}$ (which is a good enough approximation given the size of our errors; Crittenden et al. 2002; Schneider et al. 2002), and are statistically independent of the PSF when averaged over large regions. We also assume that the PSF and the intrinsic alignments are independent – but not that the lensing shear and intrinsic alignments are independent (Hirata & Seljak 2004). The two-point correlation of the galaxy shapes contains terms resulting from gravitational lensing and from systematic errors:

$$\langle ee \rangle = 4\mathcal{R}^2\xi_{\gamma,E} + \mathcal{R}_{psf}^2\xi_{psf} + \xi_{int} + \langle \gamma e_{int} \rangle. \tag{3}$$

Here, ξ_{psf} is the auto-correlation of the PSF ellipticity field. Errors in the determination of the galaxy redshift distribution will enter as a bias in the predicted $\xi_{\gamma,E}$.

Our goal is to carry out a statistics-limited measurement of $\xi_{\gamma,E}$. This will entail showing that the combined

amplitudes of $\mathcal{R}_{psf}^2\xi_{psf}$, ξ_{int}, $\langle \gamma e_{int} \rangle$, the uncertainty in the theoretically-predicted $\xi_{\gamma,E}$ arising from redshift errors, and the uncertainty in the shear calibration (via the responsivity $\mathcal{R}$) contribute less than 20 per cent to the statistical errors in $\langle ee \rangle$.

Our approach to handling of systematic error is as follows: we attempt to reduce each systematic to a term that can be robustly and believably estimated from real data (either the data here or in other, related work), and we then explicitly correct for it. These corrections naturally have some uncertainty associated with them, which we use to derive a systematic error component to the covariance matrix. The exception to the rule given here is if there is a systematic error for which there is no clear path to estimating its magnitude, then we do not attempt any correction, and simply marginalize over it by include an associated uncertainty in the covariance matrix.

3.1 Cosmic shear

Foreground anisotropies in the matter distribution along the line of sight to a galaxy will generically distort the galaxy image. For weak lensing, the leading order lensing contribution to galaxy shapes can be thought of as arising from a linear transformation of the image coordinates $\mathbf{A}x_{true} = x_{obs}$, where

$$\mathbf{A} = \begin{pmatrix} 1 + \kappa + \gamma_1 & \gamma_2 \\ \gamma_2 & 1 + \kappa - \gamma_1 \end{pmatrix}. \tag{4}$$

The convergence κ causes magnification, whereas the shear components γ_1 and γ_2 map circles to ellipses. The shear is related to the projected line-of-sight matter distribution, weighted by the lensing efficiency:

$$(\gamma_1, \gamma_2) = \partial^{-2} \int_0^\infty W(\chi, \chi_i) \left(\partial_x^2 - \partial_y^2, 2\partial_x\partial_y\right) \delta\left(\chi\hat{\mathbf{n}}_i\right) d\chi. \tag{5}$$

Here we integrate along the comoving line-of-sight distance χ (where χ_i is the distance to the source), and the matter over-density $\delta = (\rho - \overline{\rho})/\rho$. The window function in a flat universe is

$$W(\chi, \chi_i) = \frac{3}{2}\Omega_m H_0^2(1+z)\chi^2 \left(\frac{1}{\chi} - \frac{1}{\chi_i}\right). \tag{6}$$

The two-point correlation function of the shear can be calculated by identifying pairs of source galaxies, and defining shear components (γ_t, γ_x) for each one to be the shear in the coordinate system defined by the vector connecting them, and in the $\pi/4$ rotated system. This two-point correlation function can be expressed as a linear transformation of the matter power spectrum P_δ averaged over the line of sight to the sheared galaxies:

$$\begin{aligned} \xi_\pm &= \langle \gamma_t\gamma_t \rangle \pm \langle \gamma_\times\gamma_\times \rangle \\ &= \frac{1}{2\pi} \int_0^\infty d\ell\, \ell\, P_\kappa(\ell)\, J_{0,4}(\ell\theta) \end{aligned} \tag{7}$$

and

$$\begin{aligned} P_\kappa &= \left(\frac{3\Omega_m}{2d_H^2}\right) \int_0^\infty \frac{d\chi}{a(\chi)^2} P_\delta\left(\frac{\ell}{d(\chi)}\right) \\ &\times \left[\int_\chi^\infty d\chi' n(\chi') \frac{d(\chi' - \chi)}{d(\chi')}\right]^2, \end{aligned} \tag{8}$$

where the last expression makes use of Limber's approximation and $d(\chi)$ is the distance function, i.e. χ in a flat universe, $K^{-1/2} \sin K^{1/2}\chi$ in a closed universe, and $(-K)^{-1/2} \sinh(-K)^{1/2}\chi$ in an open universe. In the expression in brackets, $n(\chi')$ represents the source distribution as a function of line-of-sight distance (normalised to integrate to 1). This statistic (P_κ) is sensitive both to the distribution of matter δ and to the background cosmology, via both the explicit Ω_m dependence and the distance-redshift relations.

3.2 Intrinsic alignments

Many studies have discussed intrinsic alignments of galaxy shapes due to effects such as angular momentum alignments or tidal torque due to the large-scale density field (for pioneering studies, see Croft & Metzler 2000; Heavens et al. 2000; Catelan et al. 2001; Crittenden et al. 2001; Jing 2002; Hopkins et al. 2005). While these effects can generate coherent intrinsic alignment 2-point functions, Hirata & Seljak (2004) pointed out that the large-scale tidal fields that can cause intrinsic alignments are sourced by the same large-scale structure that is responsible for producing a cosmic shear signal. Thus, in this model, the intrinsic alignments do not just have a nonzero auto-correlation, they also have a significant anti-correlation with the lensing shear which can persist to very large transverse scales and line-of-sight separations. If left uncorrected, this coherent alignment of intrinsic galaxy shapes suppresses the lensing signal, since the response of the intrinsic shape to an applied tidal field has the opposite sign from the response of the galaxy image to a shear with the same magnitude and direction. We generally refer to the intrinsic alignment auto-correlation as the "II" contamination and its correlation with gravitational lensing as the "GI" contamination. This can be compared to the pure gravitational lensing auto-correlation ("GG").

To address the uncertainty related to intrinsic alignments, we rely on empirical measurements that constrain the degree to which they might affect our measurement. Several studies using SDSS imaging and spectroscopic data (e.g., Mandelbaum et al. 2006a; Hirata et al. 2007; Okumura et al. 2009; Joachimi et al. 2011; Mandelbaum et al. 2011b) have demonstrated the existence of intrinsic alignments of galaxy shapes on cosmological distance scales. Hirata et al. (2007) used the luminosity and colour-dependence of intrinsic alignments for several SDSS galaxy samples to estimate the contamination of the cosmic shear signal due intrinsic alignments for lensing surveys as a function of their depth. These estimates were a function of the assumptions that were made, for example about evolution with redshift. The "central" model given in that paper leads to a fractional contamination of

$$\frac{C_{\ell=500,GI}}{C_{\ell=500,GG}} \approx -0.08 \tag{9}$$

for a limiting magnitude of $m_{R,\mathrm{lim}} = 23.5$, which is close to the limiting magnitude of our sample. Subsequent work (Joachimi et al. 2011; Mandelbaum et al. 2011b) provided more information about redshift evolution; primarily those results were in broad agreement with the previous ones, and were sufficient to rule out both the "optimistic" and the "very pessimistic" models in Hirata et al. (2007).

We thus adopt the "central" model, and apply the correction given in Eq. (9) to our theory predictions for the C_ℓ due to cosmic shear, multiplying the predicted cosmic shear power spectrum by 0.92 before transforming into the statistics that are used for the actual cosmological constraints[7]. We also assume this correction has a conservative systematic uncertainty of 50 per cent, which amounts to an overall 4 per cent uncertainty in the theory prediction (see Sec. 5 for a quantitative description of how we incorporate this and other systematic uncertainties into the covariance matrix).

Since the GI correlation is first order in the intrinsic alignment amplitude, while the II power is second order, we expect the first to be the dominant systematic. In principle, the GI effect could be smaller than II if the correct alignment model is quadratic in the tidal field rather than linear (Hirata & Seljak 2004). However, in the aforementioned cases in which intrinsic alignment signals are detected at high significance (i.e. for bright ellipticals) the linear model for intrinsic alignments appears to be valid (Blazek et al. 2011). Therefore we attempt no correction for II.

3.3 Shear calibration

Another source of systematic error for weak lensing measurements is uncertainty in the *shear calibration* factor. The galaxy ellipticity $(e_+, e_\times)$ observed after isotropizing the PSF need not have unit response to shear: in general, averaged over a population of sheared galaxies, we should have

$$\langle (e_+, e_\times) \rangle = \mathcal{R}(\gamma_+, \gamma_\times), \tag{10}$$

where $\mathcal{R}$ is the shear responsivity. It depends on both the shape measurement method *and* the galaxy population (e.g. Massey et al. 2007b; Bernstein 2010; Zhang 2011).

For this work, we used the re-Gaussianization method (Hirata & Seljak 2003), which is based on second moments from fits to elliptical Gaussians, and has been previously applied to SDSS single-epoch imaging (Mandelbaum et al. 2005; Reyes et al. 2011). For this class of methods, in the absence of selection biases and weighting of the galaxies, perfectly homologous isophotes, and no noise, there is an analytic expectation (Bernstein & Jarvis 2002):

$$\mathcal{R} = 2(1 - e_{\mathrm{rms}}^2), \tag{11}$$

where e_{rms} is the root-mean-square ellipticity per component ($+$ or $\times$).

The calibration errors for re-Gaussianization and other adaptive-weighting methods are well-studied in the literature (e.g. Hirata et al. 2004b; Mandelbaum et al. 2005, 2011a; Reyes et al. 2011). They arise from all of the deviations from the assumptions of Eq. (11). Higher-order departures from non-Gaussianity in the galaxy light profile cause errors in the PSF dilution correction. Errors in the measurement of the PSF model will cause a similar error in the dilution correction. The resolution factor of an individual galaxy depends on its ellipticity, so any resolution cut on the galaxy sample will introduce a shear bias in the galaxy

---

[7] While the intrinsic alignment contamination is in principle scale-dependent, the plots in Hirata et al. (2007) suggest that this scale dependence is in fact quite weak for the scales used for our analysis, so we ignore it here.

selection function. Due to the non-linearity of the shear inference procedure, noise in the galaxy images causes a bias in the shears (rather than just making them noisier). The estimation of the shear responsivity, or even of $e_{\rm rms}$, is another potential source of error, as the response of the galaxies to the shear depends on the true, intrinsic shapes, rather than the gravitationally sheared, smeared (by the PSF), noisy ones that we observe.

Past approaches to this problem have included detailed accounting for these effects one by one. In this paper, we instead use detailed simulations of the image processing and shape measurement pipelines, including real galaxy images, to estimate both the shear calibration and the redshift distribution of our catalogue. The advantage is that this includes all of the above effects and avoids uncertainties associated with analytic estimates of errors. The SHERA (SHEar Reconvolution Analysis) simulation package[8] has been previously described (Mandelbaum et al. 2011a) and applied to single-epoch SDSS data for galaxy-galaxy lensing (Reyes et al. 2011), but this is its first application to cosmic shear data.

To simulate our images, we require a fair, flux-limited sample of any galaxies that could plausibly be resolved in our coadd imaging, including high-resolution images with realistic morphologies[9]. For this purpose we use a sample of 56 662 galaxy images drawn from the COSMOlogical Evolution Survey (COSMOS: Koekemoer et al. 2007; Scoville et al. 2007a,b) imaging catalogues. The deep *Hubble Space Telescope* (HST) Advanced Camera for Surveys/Wide Field Camera (ACS/WFC) imaging in $F814W$ ("broad I") in this 1.6 deg^2 field is an ideal source of a fairly-selected galaxy sample with high resolution, deep images[10]. These images consist of two samples – a "bright" sample of 26 116 galaxies in the magnitude range $I < 22.5$, and a "faint" sample consisting of the $22.5 < I < 23.5$ galaxies. The charge transfer inefficiency-corrected (Massey et al. 2010) and multi-drizzled (Koekemoer et al. 2002; Rhodes et al. 2007, to a pixel scale of $0.03''$) galaxy postage stamp images have been selected to avoid CCD edges and diffraction spikes from bright stars, and have been cleaned of any other nearby galaxies, so they contain only single galaxy images without image defects. The bright sample is used for ground-based image simulations in Mandelbaum et al. (2011a); the faint sample is selected and processed in an identical way[11]. Each postage stamp is assigned a weight to account for the relative likelihoods of generating postage stamps passing all cuts (avoidance of CCD edges and bright stars) for galaxies of different sizes in the COSMOS field; this weight is calculated empirically, by comparing the size distribution of galaxies with postage stamps to the size distribution of a purely flux-limited sample of galaxies.

Each of these postage-stamp images has several properties associated with it that are of interest for this analysis. The COSMOS photometric catalogues (Ilbert et al. 2009) contain HST $F814W$ magnitudes as well as photometric redshifts and Subaru $r - i$ colours based on PSF-matched aperture magnitudes.

In order to simulate our observations, we first select a coadd 'run' consisting of five adjacent frames in the scan direction at random from the list of completed runs. We draw 1250 galaxies (exactly 250 per frame) at random from the list of COSMOS postage stamps according to the weights described above, up-weighting the probability of drawing the faint galaxies by a factor of 1.106 to account for the fact that we have sampled the faint population at a lower rate than the bright one in constructing the image sample.

Once a list of postage-stamp images is selected, we assign r- and i-band magnitudes by re-scaling each image; each galaxy image is inserted into the coadded imaging with the flux it would have been observed to have in SDSS before the addition of pixel noise. The i-band is chosen to be 0.03 magnitudes brighter than the COSMOS $F814W$ (I) band `MAG_AUTO` values; this small offset is based on empirical comparison with SDSS magnitudes for brighter galaxies, to account for slight differences in the $F814W$ and i passbands (Mandelbaum et al. 2011a). The r-band is chosen so as to match the Subaru PSF-matched aperture colours for each object. Each postage stamp is assigned a random, uniformly-sampled position in the coadd run, with the postage stamps distributed equally among the frames.

We use the SHERA code to pseudo-deconvolve the HST point-spread function, apply (if necessary; see below) a shear to each galaxy, reconvolve each image with the known coadd point-spread function, renormalise the flux appropriately, and resample from the COSMOS pixel scale to the coadd pixel scale before adding that postage stamp to the coadd image. This procedure, suggested by Kaiser (2000) and implemented to high precision in Mandelbaum et al. (2011a), can be used to simulate ground-based images with a shear appropriately applied, despite the space-based PSF in the original COSMOS images, and with a user-defined PSF.

The normal coadd masking algorithm is then applied, and shear catalogues are generated as in Paper I by running the SDSS object detection and measurement pipeline, PHOTO-FRAMES, followed by the shape measurement code described in Sec. 3.3. The output catalogues are matched against the known input object positions, and a simulation catalogue of the matches is created. We employ these simulations below to determine the shear calibration and as an independent validation of our inferred redshift distribution.

For each suite of simulation realisations, we use the same random seed (i.e., we select the same galaxies from our catalogue and place them at identical locations in the coadded image) but with different applied shears per component ranging from -0.05 to $+0.05$. We measure the mean weighted shape of the detected simulation galaxies produced by our pipeline, and fit a line to the results. Since the same galaxies are used without rotation, only the slope and not the intercept is meaningful. The shear response in each component for each applied shear is shown in Fig. 1. The responsivities in the two components are consistent, which is expected on oversampled data with a rounded PSF. (The unequal size of the error bars reflects the number of runs

---

[8] `http://www.astro.princeton.edu/~rmandelb/shera/shera.html`
[9] Simple models with analytic radial profiles and elliptical isophotes are not adequate to measure all sources of systematic error such as under-fitting biases or those due to non-elliptical isophotes (Bernstein 2010).
[10] Admittedly there may be some sampling variance that affects the morphological galaxy mix.
[11] We thank Alexie Leauthaud for kindly providing these processed images.
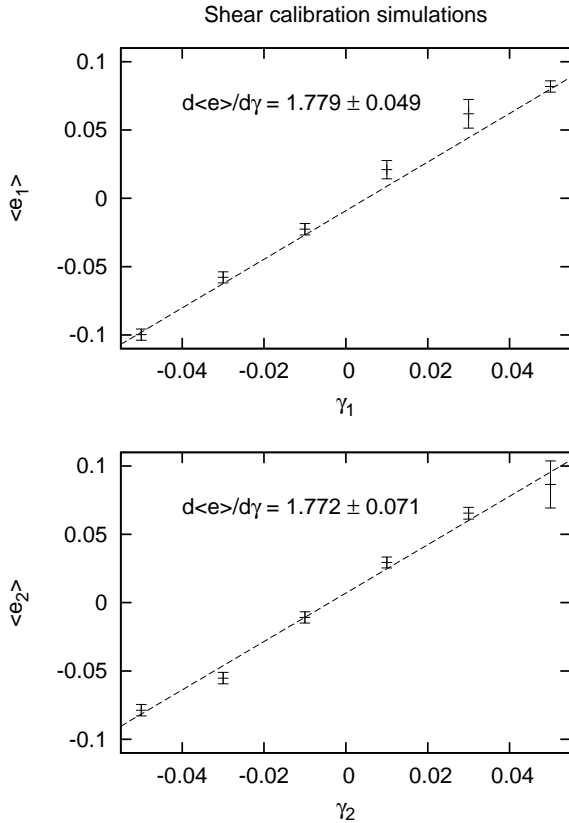
Figure 1. The response of the mean ellipticities $\langle e_1 \rangle$ and $\langle e_2 \rangle$ to applied shear, as determined in the SHERA-based simulations. Poisson error bars are shown. The additive offset to the response curve is not shown in the fit; these simulations do not accurately measure an additive shear bias.

that we were able to process by the time the shear calibration solution was frozen.) The total number of galaxies in the final simulated catalogues was 130 063. The response appears to be linear for small applied shears. Based on these results, we adopt a shear responsivity for this galaxy population of 1.776 ± 0.043.

3.4 Redshift distribution

The explicit dependence of the shear signal in Eqs. (5) and (8) on the distribution of lensed galaxy redshifts, combined with the practical impossibility of acquiring a spectroscopic redshift for the millions of faint galaxies statistically necessary for a cosmic shear measurement, can be a troublesome source of bias and systematic uncertainty for cosmic shear measurements.

An error in the estimated redshift distribution leads to an incorrect prediction for the amplitude of the shear signal at a given cosmology. This is similar in principle to the bias arising in the amplitude of the galaxy-galaxy lensing signal due to photometric redshift biases explored in Nakajima et al. (2011); uncorrected, standard photometric redshift estimation techniques can lead to biases in the predicted lensing signal at the ~ 10 per cent level. For cosmic shear measurements, an imperfect estimate of the redshift distribution leads to biases in σ_8 and Ω_m that are compara-

ble in amplitude to the errors in the estimated mean of the redshift distribution (van Waerbeke et al. 2006).

As a fiducial reference, the redshift distribution of the single-epoch SDSS imaging catalogue is established to approximately 1 per cent (Sheldon et al. 2011); for deeper surveys over a smaller area, this becomes a more difficult problem, as the spectroscopic calibration samples available for inferring the redshift distribution are limited in their redshift coverage and widely dispersed across the sky. We employ a colour-matching technique similar to that employed by Sheldon et al. (2011); in what follows, we describe the technique, our estimate of its uncertainty, and several crosschecks on the results.
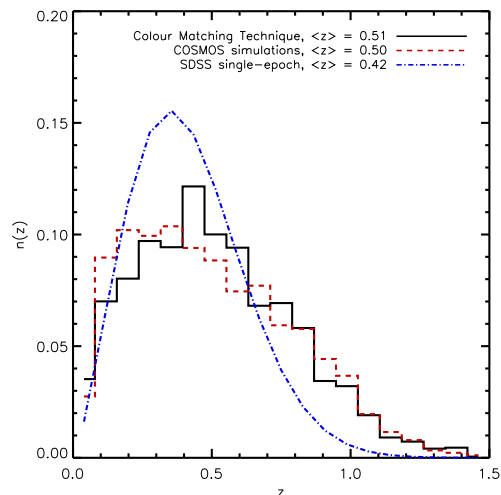
3.4.1 Fiducial redshift distribution

The source redshift distribution used in our analysis is derived following Lima et al. (2008) and Cunha et al. (2009), and is similar in spirit to Sheldon et al. (2011); the principle is that, for two galaxy samples that span broadly similar ranges in redshift, colour, and limiting magnitude, matched colour samples correspond to matched redshift distributions.

Our spectroscopic calibration sample is composed of 12 360 galaxies, from the union of the VIMOS VLT Deep Survey (Le Fèvre et al. 2005, VVDS) 22h field, the DEEP2 Galaxy Redshift Survey (Davis et al. 2003; Madgwick et al. 2003), and portions of the PRism MUlti-object Survey (PRIMUS; Coil et al. 2011, Cool et al. 2011 *in prep.*). We follow the procedures outlined in Nakajima et al. (2011) for selecting good quality spectroscopic redshifts, and avoiding duplicate galaxies in samples that overlap (such as DEEP2 and PRIMUS). Each of these samples has a redshift distribution that is likely to differ substantially from the redshift distribution of our lensing catalogue: the DEEP2 catalogue in the fields we use at $23^h 30^m$ and $02^h 30^m$ is heavily colour-selected (in non-SDSS bands) towards objects at $z > 0.7$; the PRIMUS catalogue includes several fields, some of which are selected from imaging with a shallower limiting magnitude; and the VVDS catalogue is selected in the I band ($I < 22.5$) with a relatively high redshift failure rate that exhibits some colour dependence.

We assign a redshift from a galaxy in the union calibration sample to the closest galaxy in the lensing catalogue within 3 arcsec, finding 12 360 matches. To generate a representative training sample of galaxies from the lens catalogue, we draw 4×10^5 galaxies with replacement from the full area (not just in these regions), with sampling probability proportional to the mean of the weights assigned in the r and i bands to that galaxy for the correlation analysis (Eq. 17). Note that this procedure does not incorporate those galaxies in the excluded camcol 2 region.

We use the Lima et al. (2008) code[12] to solve for a set of weights over the calibration sample, such that the reweighted 5-dimensional magnitude distributions of the calibration sample match those of the representative random subset of the lensing catalogue. The histogram of the calibration sample redshifts reweighted in this manner is shown as a solid line in Fig. 2. The inferred mean redshift is 0.51; in

---

[12] http://kobayashi.physics.lsa.umich.edu/~ccunha/nearest/

$$n_{\text{eff},i,j} = \sum_k w_{nn,i,j,k} \tag{13}$$

To propagate these errors into the covariance matrix for ξ_E, we first fit a smooth function of the form

$$n_z(z) \propto z^a e^{-(z/z_0)^b} \tag{14}$$

to the nearest neighbour weighting-derived redshift distribution shown in Figure 2; the best fit parameters are $a = 0.5548$, $z_0 = 0.7456$, and $b = 2.5374$. We perturb this smooth distribution by adding a random number drawn from a normal distribution with mean $n_z(z_j)$ (normalised to the weighted number of calibration galaxies in that bin) and standard deviation σ_j at the location of the jth redshift bin. We then renormalise the perturbed distribution to unity, and compute the predicted cosmic shear signal. The covariance matrix of 402 realisations of this procedure is added to the statistical covariance matrix.

3.4.3 Other tests

As an independent check on the redshift distribution, we also use the shear calibration simulations (Sec. 3.3) to constrain the redshift distribution of our sources. The COSMOS photometric redshifts, inferred as they are from many more imaging bands (typically with deeper imaging) than for the SDSS data discussed here, are very accurate. For example, Ilbert et al. (2009) finds a photo-z scatter of $\sigma_z/(1+z) \sim 0.01$ for a galaxy sample with the flux limit of the SDSS coadds. In contrast, Nakajima et al. (2011) found that in the SDSS single-epoch imaging, the scatter defined in the same way was ~ 0.1 despite the brighter flux limit of the single-epoch imaging (due in part to the more limited number of bands, but primarily to the far lower signal-to-noise ratio). If we treat the COSMOS photometric redshifts as we would spectroscopic data, then the redshift distribution of COSMOS galaxies that pass successfully into the shear catalogue is the same as that of our source catalogue – assuming, of course, that the COSMOS field is representative of the whole of Stripe 82. It is not, of course; large-scale structure in the COSMOS field (which can be significant, as COSMOS covers only 1.7 square degrees; Kovač et al. 2010) can bias a determination of the redshift distribution in this manner. The $n(z)$ inferred from the COSMOS-based simulations is also shown in Fig. 2, and agrees extremely well with the fiducial $n(z)$ derived from colour-matching.

A final (but obviously not independent) sanity check is to compare to the COSMOS Mock Catalogue (Jouvel et al. 2009), which is being used extensively to plan future dark energy programmes, using the cuts $r_{\text{eff}} > 0.47$ arcsec, limiting magnitudes $r < 23.5$, and $i < 22.5$ (see Paper I, where we argue that these most closely mimic the cuts in our data). This test predicts $\langle z \rangle = 0.51$, identical to that obtained via the re-weighting procedure. Given the crudeness of the procedure for comparing the results, this is an excellent validation of the COSMOS Mock Catalogue as a forecasting tool.

3.5 Stellar contamination

Stellar contamination of the galaxy catalogue reduces the apparent shear by diluting the signal with round objects that

Figure 2. The redshift distribution inferred from matching the colours of the spectroscopic calibration sample to those of the lensing catalogue (solid black line, Sec. 3.4.1) shown alongside the noisier redshift distribution inferred from the shear calibration simulations (dashed red line, Sec. 3.4.3). The best-fit distribution for the single-epoch SDSS lensing catalogue from Nakajima et al. (2011) is shown for reference as the blue dot-dashed line.

contrast to the redshift distribution for single-epoch imaging, there is a non-negligible fraction of the galaxy sample above $z > 0.7$. We use the solid curve based on the colour-matching techniques to calculate the shear covariance matrix, and to predict the shear correlation function for any given cosmology.

3.4.2 Uncertainty

We expect that the primary source of error in the redshift distribution as estimated from the combined calibration sample is sample variance, resulting from the finite volume of the calibration sample. To estimate its magnitude, we use the public code of Moster et al. (2011) for estimating the cosmic variance of number counts in small fields.

Our redshift binning scheme has 19 bins between $0 < z < 1.5$. For a collection of disparate calibration fields, we use the Moster et al. (2011) code to produce a fractional error in the number counts $\sigma_{\text{gg},i,j}$ for the jth redshift bin in the i field (where fields are distinguished by their coverage area) in bins of stellar mass.

The redshift sampling rate of each distinct survey in the calibration sample differs, and so the balance of contributions to the final redshift distribution will change as well. To account for this, we sum over every calibration field's contribution to the reweighted redshift distribution in the j bin to estimate an absolute (not relative) overall error:

$$\sigma_j^2 = \sum_i (\sigma_{\text{gg},i,j} n_{\text{eff},i,j})^2 \tag{12}$$

where the effective number of galaxies contributed in the j bin by the i survey is just the sum over the nearest-neighbour derived weights assigned to calibration sample galaxies k in that field i and bin j:

are not sheared by gravitational lensing. Because the image simulations described in Sec. 3.3 only included galaxies, the resulting shear responsivities do not include signal dilution due to accidental inclusion of stars in the galaxy sample. In Paper I, we estimated the stellar contamination by comparison with the DEEP2 target selection photometry (which is deeper and was acquired at the Canada-France-Hawaii Telescope under much better seeing conditions than typical for SDSS), and found a contamination fraction of 0.017. We also argued that the mean stellar density in the stripe must be larger than in the high-latitude DEEP2 fields, by a factor as large as 2.8. We therefore conservatively take the stellar contamination fraction $f_{\rm star}$ to be

$$f_{\rm star} = 0.017(1.9 \pm 0.9) = 0.032 \pm 0.015. \qquad (15)$$

The resulting suppression of the cosmic shear signal is treated in much the same way as for intrinsic alignments: we reduce the theory signal by a factor of $(1 - 0.032)^2 = 0.936$, and add a contribution to the covariance of 0.030 times the theory signal.

3.6 Additive systematics

Among the most worrying systematics in the early detections of cosmic shear was additive power. This comes from any non-cosmological source of fluctuations in shapes such as PSF anisotropy that add to the ellipticity correlation function of the galaxies. Such power was clearly detected in Paper I in the form of systematic variation of both star and galaxy e_1 as a function of declination. The sense of the effect – a negative contribution to e_1 (in r band we have[13] $\langle e_1 \rangle = -0.0018$ and $\langle e_2 \rangle = +0.0004$, while in i band $\langle e_1 \rangle = -0.0022$ and $\langle e_2 \rangle = -0.0002$) – is suggestive of *masking bias*, in which the selection of a galaxy depends on its orientation, with galaxies aligned in the along-scan direction ($e_1 < 0$) being favoured, and with no effect on e_2 (consistent with zero mean over the whole survey). The reason for this particular sign is seen in Figure 2 of Paper I; as shown, bad columns along the scan direction tend to be repeated at the same location in multiple images, resulting in significant (non-isotropic) masks with that directionality. Direct evidence for masking bias comes from the change in mean ellipticity due to increased masking: when we removed from the coadded image pixels that were observed in fewer than 7 input runs and reran PHOTO-FRAMES, the $\langle e_1 \rangle$ signal became *worse*: -0.0051 in r band and -0.0044 in i band, whereas $\langle e_2 \rangle$ was essentially unchanged. This increase is difficult to explain in terms of spurious PSF effects, so we conclude that our galaxy catalogue likely contains a mixture of masking bias as well as possible additive systematics from PSF ellipticity in the coadded image.

The mean e_1 signal as a function of declination is shown in Fig. 3 in bins of width 0.05 degrees. We take this as a template for mask-related selection biases (combined with any systematic uncorrected PSF variation as a function of declination, which in west-to-east drift-scan observations is a highly plausible type of position dependence). *Before com-*

---

[13] The 1σ Poisson uncertainty in these numbers is 0.0005 (0.0004) per component in r (i) band.
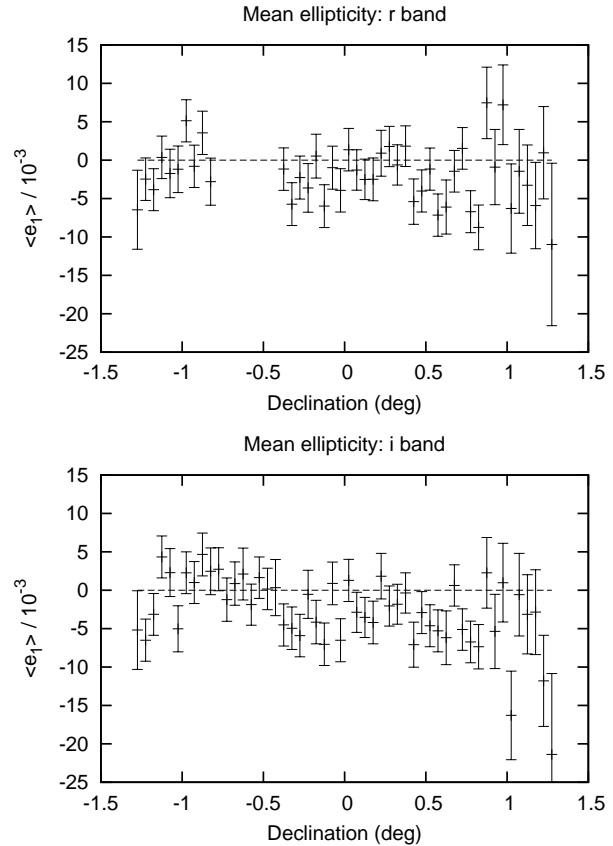
Figure 3. The mean ellipticity $\langle e_1 \rangle$ as a function of declination in the r and i bands. This signal was removed from the galaxy catalogue prior to computing the final correlation function. The r band data between declination $-0.8°$ and $-0.4°$ were rejected due to the known problems with camcol 2. The error bars are Poisson errors only.

puting the correlation function, we subtracted this mean signal from the galaxy ellipticity catalogue.
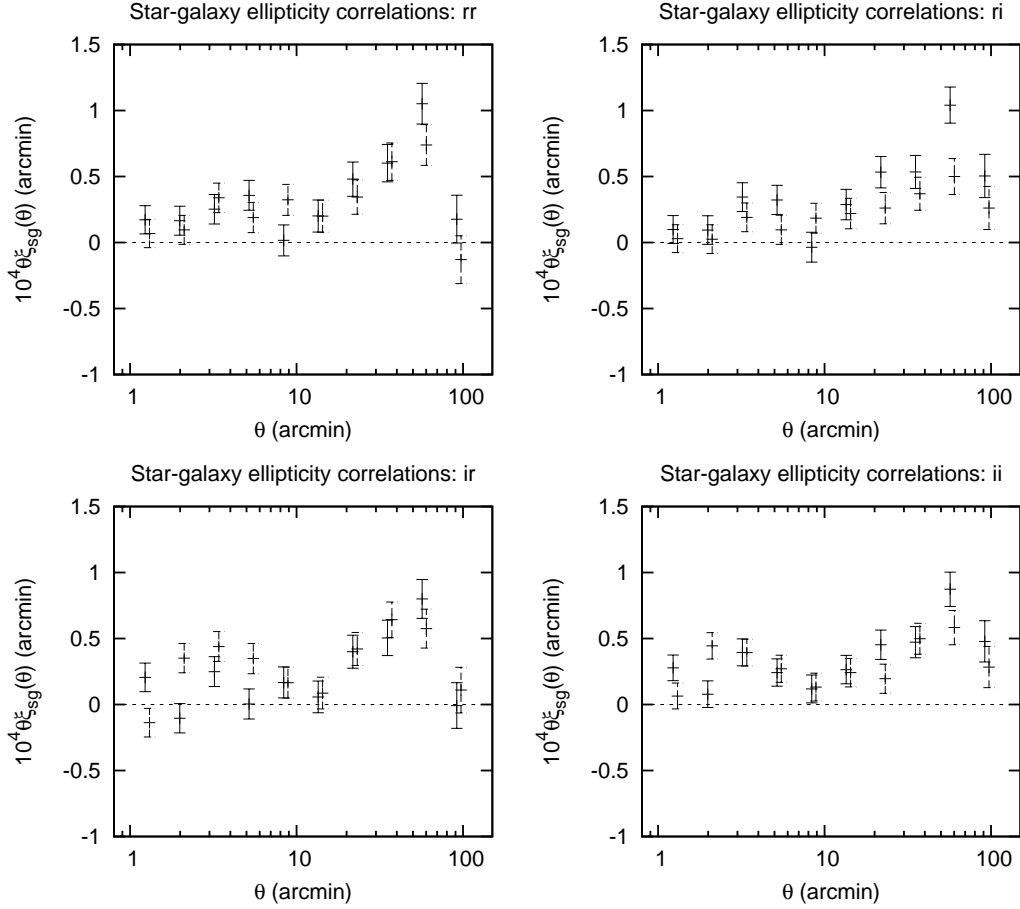
One danger in this procedure to remove spurious $\langle e_1 \rangle$ is that some real power could be removed – that is, even in the absence of any systematic error, some of the actual galaxy shape correlation function signal could be suppressed since the method determines the mean e_1 of the real galaxies and by subtracting it introduces a slight artificial anti-correlation. The best way to guard against this is with simulations. Using the Monte Carlo simulation tool of Sec. 5.1.2, we generated simulated realisations of our ellipticity catalogue and either implemented the $\langle e_1 \rangle$ projection or not. The difference in the correlation functions is a measure of how much power was removed. The result is shown in Fig. 4, and shows that the loss of real power is insignificant compared to our error bars.

3.6.1 PSF anisotropy

Convolution with an elliptical PSF will induce a spurious ellipticity in observed galaxy surface-brightness profiles. While the effective PSF for these coadds is a circular double Gaussian to quite high precision, the tests in Paper I indicate a low level of residual anisotropy that we must consider here.

Figure 5. The star-galaxy ellipticity correlation functions. Shown are the rr, ri (i.e. star $r \times$ galaxy i), ir, and ii correlation functions, reduced to 10 bins. The solid points, which are offset to slightly lower θ-values for clarity, are the $++$ correlation functions, and the dashed points are the $\times\times$ functions. All error bars are Poisson only.
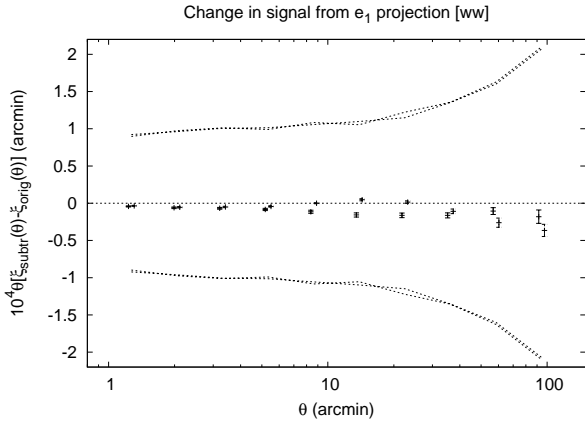
Figure 4. The loss of actual power due to e_1 projection. Using 36 realizations from the Monte Carlo simulation, we find the difference in post-projection ellipticity correlation function $\xi(\theta)$ and original $\xi(\theta)$. These are shown as the solid points (ξ_{++}) and dashed points ($\xi_{\times\times}$) in the figure, re-binned to 10 bins in angular separation θ. The dashed lines at top and bottom are the $\pm 1\sigma$ statistical error bars of our measurement. The reduction of actual power is detectable by combining many simulations, but is very small compared to the error bars on the measurement.

Possible sources of this issue include: (i) inaccuracies in the single-epoch PSF model used to determine the kernel to achieve the desired PSF; (ii) colour-dependence of the PSF that means the single-epoch PSF model from the stars is not exactly the PSF for the galaxies; or (iii) the fact that we determine the rounding kernel on a fixed grid, so that smaller-scale variations in PSF anisotropy might remain uncorrected. All of these must be present at some level, although the last two cannot be the full solution: (ii) does not explain the residual stellar ellipticity[14], and (iii) does not explain why there is structure in the declination direction on the scale of an entire CCD (0.23 degrees).

For a galaxy and a PSF that are both well-approximated by a Gaussian, the PSF-correction given above produces a measured ellipticity of:

$$e^{\mathrm{obs}} = \mathcal{R}_{\mathrm{psf}} e^{\mathrm{PSF}} = \frac{1 - R_2}{R_2} e^{\mathrm{PSF}}; \qquad (16)$$

see e.g. Bernstein & Jarvis (2002). The weighted (by the

---

[14] We have searched for a $g - i$ dependence in the stellar ellipticities in the coadded image. We only found effects at the ~ 0.002 level, and while they are statistically significant, we have not established whether they correspond to true colour dependence versus e.g. variation of stellar colour distributions along the stripe.
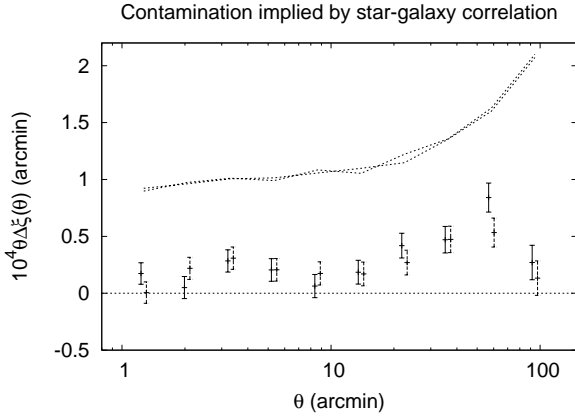
Figure 6. The implied contamination to the galaxy ellipticity correlation function if the star-galaxy correlation function is used as a measure of the additive PSF power. The solid points are the $++$ correlation functions, and the dashed points are the $\times\times$ functions. All error bars are propagated from the Poisson errors assuming correlation coefficient $+1$ (a better assumption than independent errors, but likely an overestimate). The dotted curves show the 1σ errors in each radial bin from the Monte Carlo simulations (see Sec. 5.1.2) which include both Poisson and cosmic variance uncertainties. Note also that the shapes and normalisations of the $++$ and $\times\times$ signals are nearly identical.

same weights used for the correlation function; see Eq. 17) average of the PSF anisotropy response defined in Eq. (2) over the sample of galaxies considered in this work is $\mathcal{R}_{\mathrm{psf}} = 0.86$ (r band) or 0.95 (i band); in what follows we take a value of 0.9.

A nonzero star-galaxy correlation function ξ_{sg} resulting from systematic PSF anisotropy (as estimated in Paper I) indicates the presence of a spurious contribution to the shear-shear correlation function with amplitude $\approx 0.9\xi_{\mathrm{sg}}$. We will not determine this response to high enough accuracy to subtract the effect with small residual error: doing so would not require just a simulation, but a simulation that knows the correct radial profile of the PSF errors.[15] In our case, the star-galaxy correlation function is detectable but below the errors on the galaxy-galaxy ellipticity auto-correlation (although not by very much), so a highly accurate correction is unnecessary.

We constrain the PSF anisotropy contribution by computing the star-galaxy correlation function. This was done in Paper I, but some of the star-galaxy signal is due to the systematic variation of PSF ellipticity with declination and is removed by the subtraction procedure above. The star-galaxy ellipticity correlation function with the corrected catalogue is shown in Fig. 5. The implied contamination to the galaxy ellipticity correlation function, appropriately averaging the bands and applying the factor of $\mathcal{R}_{\mathrm{psf}} = 0.9$, is shown in Fig. 6.

These measured star-galaxy correlations can be used

---

[15] This might be an option in future space-based surveys if the type of error can be traced to the source of ellipticity (astigmatism×defocus, coma, or jitter). In either space or ground-based data, one could imagine doing cross-correlations of higher-order shapelet modes (Refregier 2003) to extract the particular form of the errors. None of these options are pursued here.

to construct a reasonable systematics covariance matrix for this systematic. We take the amplitude of the diagonal elements of the PSF systematic covariance to be equal to the amplitude of the measured contamination. We also assume that the off-diagonal terms are fully-correlated between bins, which is equivalent to fixing the scaling of this systematic with radius, and saying that only the overall amplitude of the systematic is uncertain.

Since there are a number of uncertainties in this procedure, we do not apply any correction for these additive PSF systematics as we do for ones that are previously discussed, such as intrinsic alignments or stellar contamination. Instead, we simply include a term in the systematics covariance matrix to account for it. We also will present a worst-case scenario for the impact of this term on cosmological constraints; in Sec. 6 we will show what happens to the cosmology constraints if we assume that the systematic error is $+2\sigma$ from its mean, i.e. 40 per cent of the statistical errors. This should be taken as a worst-case scenario for this particular systematic.

# 4 ANALYSIS TOOLS

4.1 Ellipticity correlation function

We compute the ellipticity correlation functions defined in Eq. (7) on scales from 1–120 arcminutes. For the cosmological analysis, we start by computing the correlation function in 100 bins logarithmically spaced in separation θ to avoid bin width artifacts. For the cosmological parameter constraints, we project these onto the Complete Orthogonal Sets of E-/B-mode Integrals (COSEBI) basis (Schneider et al. 2010) to avoid the instabilities of inverting a large covariance matrix estimated via Monte Carlo simulations (we will describe our implementation of COSEBIs in Sec. 4.3). However, for display purposes, it is more convenient to reduce the θ resolution to only 10 bins so that the real trends are more visually apparent.

4.1.1 Weighting

The correlation functions used here are weighted by the inverse variance of the ellipticities, where the "variance" includes shape noise. Specifically, we define a weight for a galaxy

$$w_i = \frac{1}{\sigma_e^2 + 0.37^2}, \tag{17}$$

where σ_e is the ellipticity uncertainty per component defined by our shape measurement pipeline. As demonstrated by Reyes et al. (2011), these may be significantly underestimated in certain circumstances; however, this will only make our estimator slightly sub-optimal, so we do not attempt to correct for it. The value of 0.37 for the root-mean-square (RMS) intrinsic ellipticity dispersion per component comes from the results of Reyes et al. (2011), for $r < 22$, and therefore we are implicitly extrapolating it to fainter magnitudes. Given that Leauthaud et al. (2007) found a constant RMS
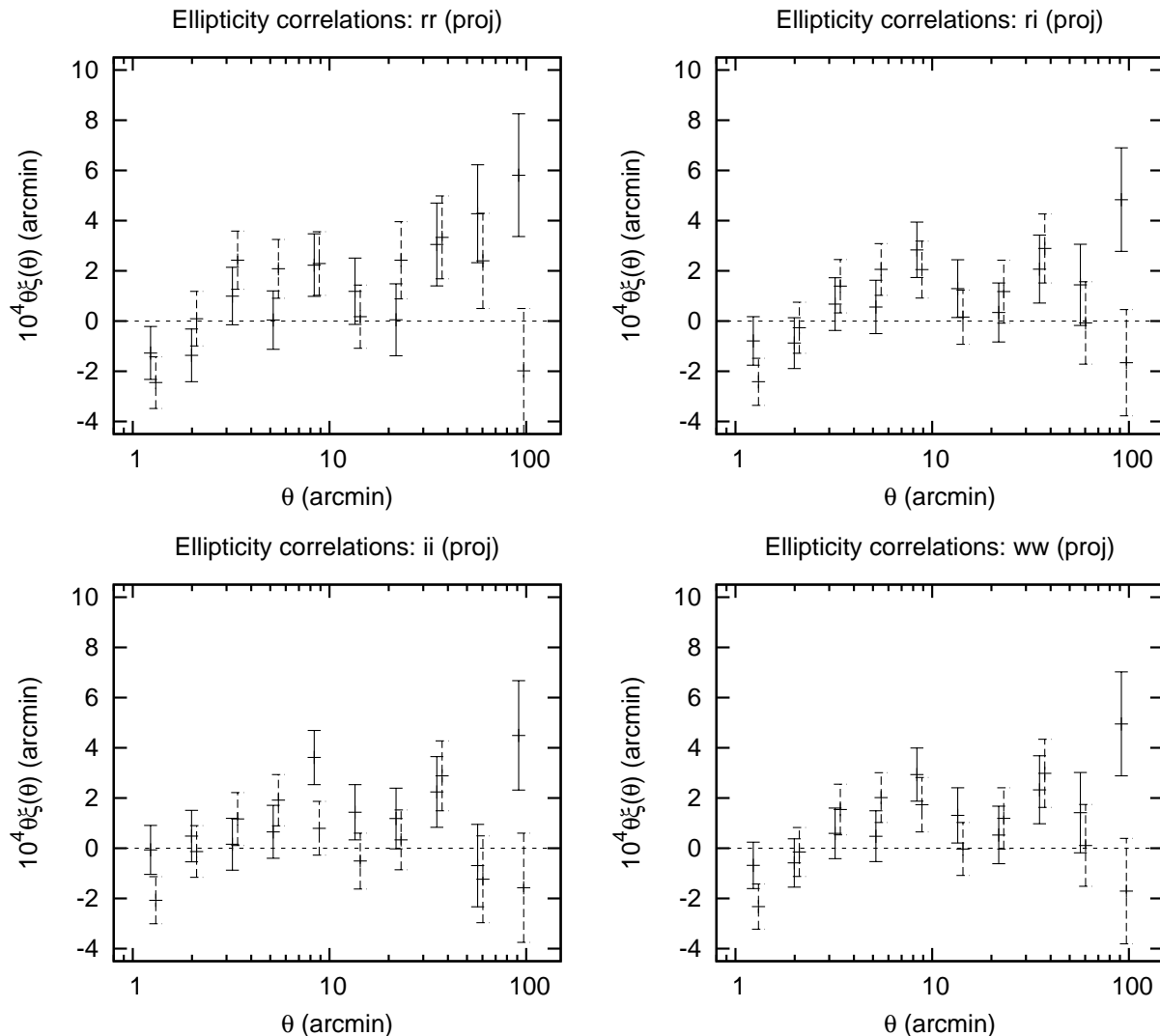
Figure 7. The ellipticity correlation functions in the rr, ri, ii and ww (combined) band combinations. The solid points denote the $++$ and the dashed points denote the $\times\times$ components of the correlation function. The points have been slightly displaced horizontally for clarity. The Monte Carlo errors are shown.

ellipticity to far fainter magnitudes in the COSMOS data, we consider this extrapolation justified[16].

4.1.2 Direct pair-count code

A direct pair-count correlation function code was used for the cosmological analysis. It is slow (~ 3 hours for 2×10^6 galaxies on a modern laptop) but robust and well-adapted to the Stripe 82 survey geometry. The code sorts the galaxies in order of increasing right ascension α; the galaxies are assigned to the range $-60° < \alpha < +60°$ to avoid unphysical edge effects near $\alpha = 0$. It then loops over all pairs with

---

[16] Note that we do not use the actual value of RMS ellipticity from Leauthaud et al. (2007) – only the trend with magnitude – because, as demonstrated by Mandelbaum et al. (2011a), the RMS ellipticity value in Leauthaud et al. (2007) is not valid for our adaptively-defined moments, which use an elliptical weight function matched to the galaxy light profile.

$|\alpha_1 - \alpha_2| < \theta_{max}$. The usual ellipticity correlation functions can be computed, e.g.

$$\xi_{++}(\theta) = \frac{\sum_{ij} w_i w_j e_{i+} e_{j+}}{\sum_{ij} w_i w_j}, \tag{18}$$

where the sum is over pairs with separations in the relevant θ bin, and the ellipticity components are rotated to the line connecting the galaxies. The direct pair-count code works on a flat sky, i.e. equatorial coordinates (α, δ) are approximated as Cartesian coordinates. This is appropriate in the range considered, $|\delta| < 1.274°$, where the maximum distance distortions are $\frac{1}{2}\delta_{max}^2 = 2.5 \times 10^{-4}$. The direct pair-count code is applicable to either auto-correlations of galaxy shapes measured in a single filter (rr, ii) or cross-correlations between filters or between distinct populations of objects (ri and all of the star-galaxy correlations).

Simple post-processing allows one to compute the ξ_+ and ξ_- correlation functions, defined by

$$\xi_+(\theta) \equiv \xi_{++}(\theta) + \xi_{\times\times}(\theta) \tag{19}$$

and

$$\xi_-(\theta) \equiv \xi_{++}(\theta) - \xi_{\times\times}(\theta). \tag{20}$$

4.1.3　Combining bands

Finally, the different band correlation functions rr, ri, and ii must be combined according to some weighting scheme:

$$\xi_{++}^{ww}(\theta) = w_{rr}\xi_{++}^{rr}(\theta) + w_{ri}\xi_{++}^{ri}(\theta) + w_{ii}\xi_{++}^{ii}(\theta), \tag{21}$$

where the label "ww" indicates that the bands were combined. The relative weights were chosen according to the fraction of measured shapes in r- and i-bands, i.e. $w_{rr} = f_r^2$, $w_{ri} = 2f_r f_i$, and $w_{ii} = f_i^2$ where the weights are $f_r = 0.4603$ and $f_i = 0.5397$.

The final ellipticity correlation functions (with the θ resolution reduced to 10 bins) are shown in Fig. 7.

4.2　Tests of the correlation function

We implement several null tests on the correlation function to search for remaining systematic errors.

The first test, shown in Fig. 8, constructs the difference between the cross-correlation function of r and i band galaxy ellipticities versus the rr and ii auto-correlations. The differences in the two types of correlation functions are small compared to the statistical uncertainty in the signal. This is consistent with our expectations, as the true cosmic shear signal should be independent of the filters in which galaxy shapes are measured.

The second test, shown in Fig. 9, compares the (band averaged or ww) correlation function computed using galaxy pairs separated in the cross-scan (north-south) direction versus pairs separated in the along-scan (east-west) direction. This difference should be zero if the signal we measure is due to lensing in a statistically isotropic universe. The error bars shown are Poisson errors, so they may be slight underestimates at the larger scales, where cosmic variance becomes important. Visual inspection shows no obvious offset from zero, but the error bars are larger for this test than in Fig. 8 because the null test includes no cancellation of galaxy shape noise.

4.3　E/B-mode decomposition

As a final check for systematics, we decompose the 2-point correlation function (2PCF) into E- and B-modes, where, to leading order, gravitational lensing only creates E-modes. The B-modes can arise from the limited validity of the Born approximation (Jain et al. 2000; Hilbert et al. 2009), redshift source clustering (Schneider et al. 2002), and lensing (magnification) bias (Schmidt et al. 2009; Krause & Hirata 2010), however the amplitude of B-modes from these sources should be undetectable with our data. At our level of significance, a B-mode detection would indicate remaining systematics, e.g. due to spurious power from an incomplete PSF correction.

Formerly used methods to decompose E-and B-modes, such as the aperture mass dispersion

$$\langle M_{\mathrm{ap}}^2 \rangle(\theta) = \int_0^{2\theta} \frac{\mathrm{d}\vartheta\,\vartheta}{2\,\theta^2} \left[\xi_+(\vartheta)T_+\left(\frac{\vartheta}{\theta}\right) + \xi_-(\vartheta)T_-\left(\frac{\vartheta}{\theta}\right) \right], \tag{22}$$
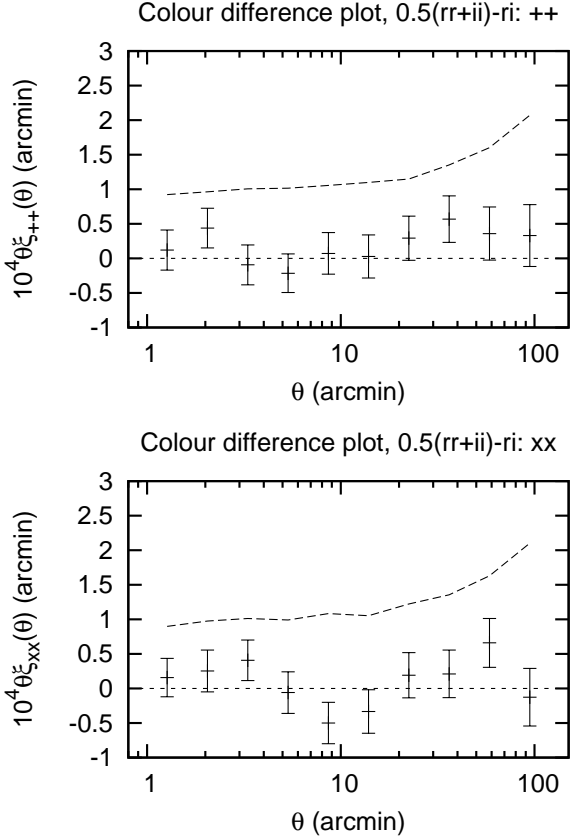
Figure 8. The difference between the galaxy ellipticity cross-correlations (ri) and the auto-correlations ($rr + ii$)/2, with error bars determined from the Monte Carlo simulations. The upper panel shows the $++$ correlations and the lower panel shows the $\times\times$ correlations. The dashed line is the 1σ statistical error bar on the actual signal.

with the filter functions $T_\pm$ as derived in Schneider et al. (2002), or the shear E-mode correlation function, suffer from E/B-mode mixing (Kilbinger et al. 2006), i.e. B-modes affect the E-mode signal and vice versa. These statistics can be obtained from the measured 2PCF, for an exact E/B-mode decomposition, however they require information on scales outside the interval $[\theta_{\min}; \theta_{\max}]$ for which the 2PCF has been measured.

The ring statistics (Schneider & Kilbinger 2007; Eifler et al. 2010; Fu & Kilbinger 2010) and more recently the COSEBIs (Schneider et al. 2010) perform an EB-mode decomposition using a 2PCF measured over a finite angular range. COSEBIs and ring statistics can be expressed as integrals over the 2PCF as

$$EB = \int_{\theta_{\min}}^{\theta_{\max}} \frac{\mathrm{d}\theta}{2}\,\theta[T_{+n}^{\log}(\theta)\xi_+(\theta) \pm T_{-n}^{\log}(\theta)\xi_-(\theta)] \tag{23}$$

and

$$R_{\mathrm{EB}}(\theta) = \int_{\theta_{\min}}^{\theta} \frac{\mathrm{d}\theta'}{2\theta'}[\xi_+(\theta')Z_+(\theta',\theta) \pm \xi_-(\theta')Z_-(\theta',\theta)]. \tag{24}$$

For the ring statistics, we use the filter functions $Z_\pm$ specified in Eifler et al. (2010). The derivation of the COSEBI filter functions $T_{\pm n}$ is outlined in Schneider et al. (2010), where the authors provide linear and logarithmic filter func-
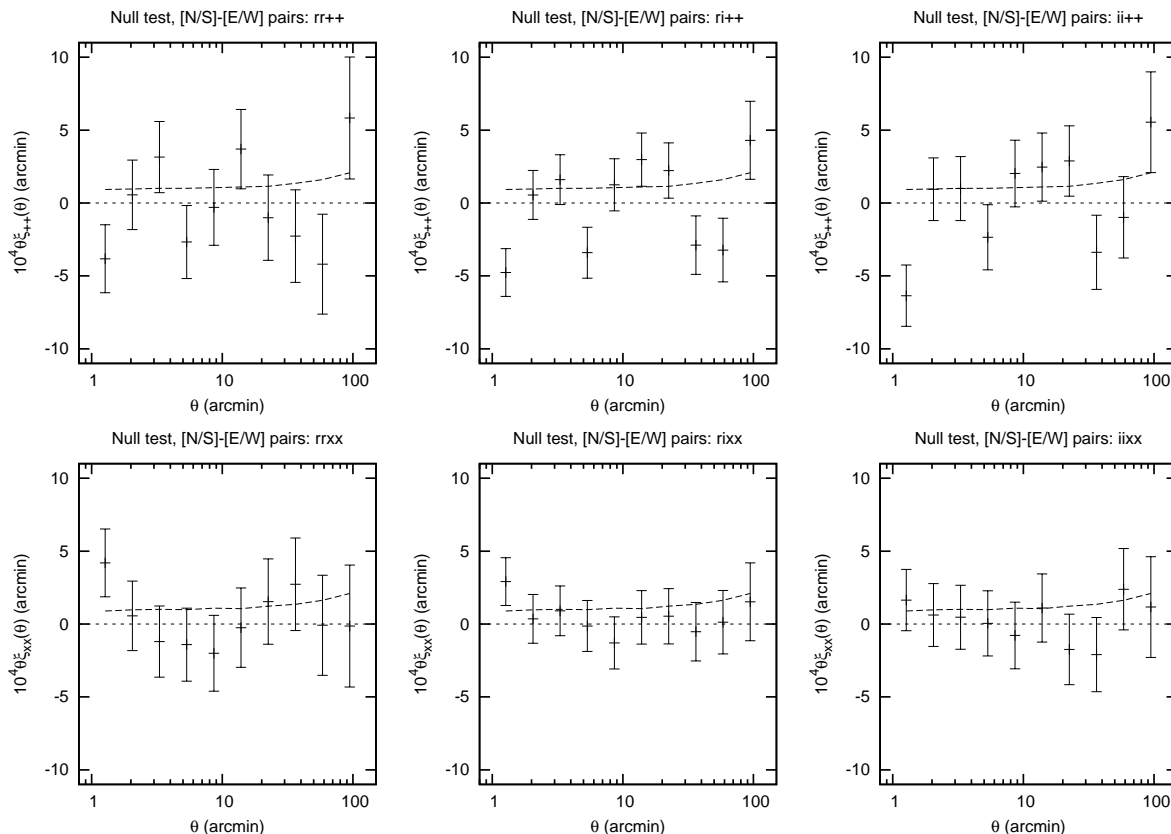
Figure 9. The null test of the correlation functions measured using galaxy pairs whose separation vector is within 45° of the north-south direction, minus that measured using galaxy pairs whose separation vector is within 45° of the east-west direction. The error bars shown are the Poisson errors only. The dashed curve shows the 1σ error bars of the actual signal (all colour combinations and separation vectors averaged). The 6 panels show the three colour combinations (rr, ri, and ii) and the 2 components ($++$ or $\times\times$).

tions indicating whether the separation of the roots of the filter function is distributed linearly or logarithmically in θ. Note that whereas the ring statistics are a function of angular scale, the COSEBIs are calculated over the total angular range of the 2PCF, condensing the information from the 2PCF naturally into a set of discrete modes. The linear T-functions can be expressed conveniently as Legendre polynomials, however $T_{\pm n}^{\log}$ compresses the cosmological information into significantly fewer modes; we therefore choose the logarithmic COSEBIs as our second-order shear statistic in the likelihood analysis in Sec. 6. The COSEBI filter functions are displayed graphically in Fig. 10.

Figure 11 shows three different E/B-mode statistics derived from our measured shear-shear correlation function, i.e. the COSEBIs, the ring statistics, and the aperture mass dispersion. The error bars are obtained from the square root of the corresponding covariances' diagonal elements (statistics only). Note that the COSEBIs data points are significantly correlated. Slightly smaller is the correlation for the aperture mass dispersion, and the ring statistics' data points have the smallest correlation.

From the COSEBIs, we find a reduced χ^2 for the E-modes to be consistent with zero of 6.395, versus 1.096 for the B-modes (5 degrees of freedom each). The latter is consistent with purely statistical fluctuations.

5 COVARIANCE ESTIMATION

5.1 Ellipticity correlation function covariance matrix

The covariance matrix of the ellipticity correlation function estimated via Eq. (21) was computed in several ways. The preferred method for our analysis is a Monte Carlo method (Sec. 5.1.2) but we compare that covariance matrix with an estimate of the Poisson errors (Sec. 5.1.1) as a consistency check.

5.1.1 Poisson method

The direct pair-count correlation function code can compute the Poisson error bars, i.e. the error bars neglecting the correlations in $e_{i+}e_{j+}$ between different pairs. This estimate of the error bar is

$$\sigma^2[\xi_{++}(\theta)] = \frac{\sum_{ij} w_i^2 w_j^2 |e_i|^2 |e_j|^2}{2\left[\sum_{ij} w_i w_j\right]^2}. \qquad (25)$$

Equivalently, this is the variance in the correlation function that one would estimate if one randomly re-oriented all of the galaxies. The Poisson method is simple, however it is not fully appropriate for ri cross-correlations (since the same intrinsic shape noise is recovered twice for pairs that appear in both ri and ir cross-correlations). Moreover, at scales of
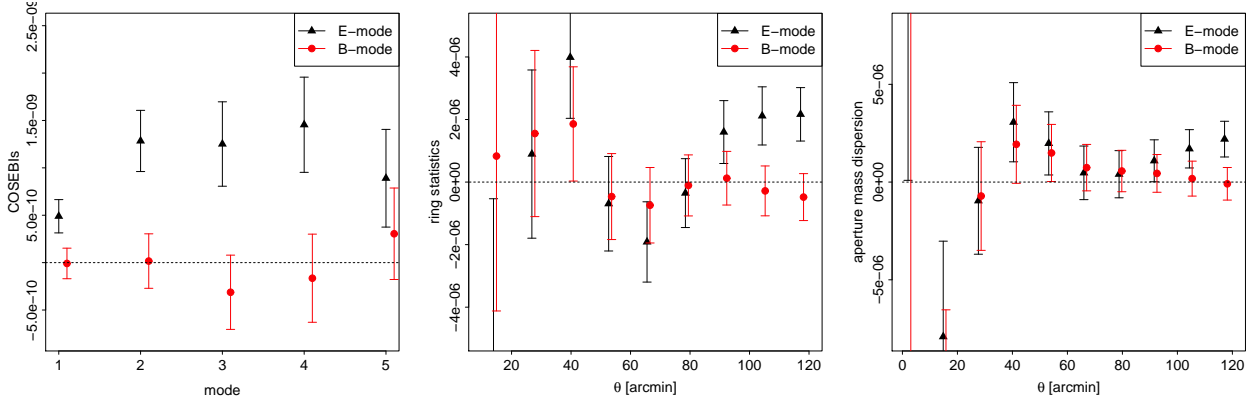
Figure 11. The measured COSEBIs, ring statistics, and aperture mass dispersion from the combined cosmic shear signal. The error bars equal the square root of the corresponding covariances' diagonal elements (statistics only). Note that the COSEBIs data points are significantly correlated. Slightly smaller is the correlation for the aperture mass dispersion, and the ring statistics' data points have the smallest correlation.
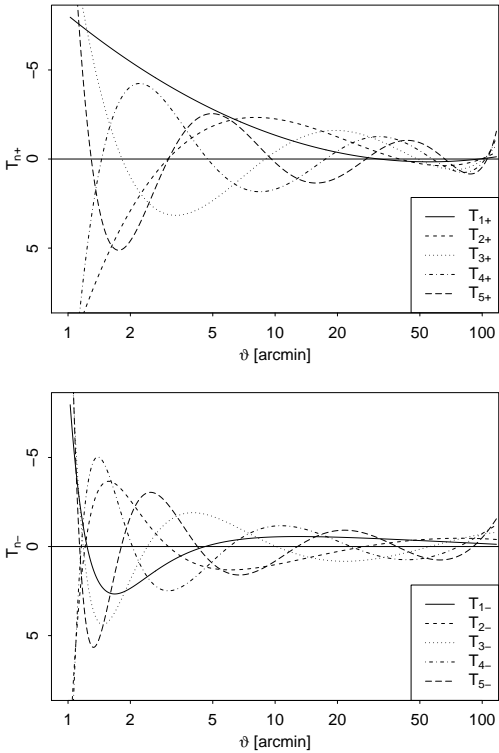
Figure 10. The COSEBI filter functions T_{n+} (upper panel) and T_{n-} (lower panel) for the first 5 modes.

tens of arcminutes and greater there is an additional contribution because the cosmic shear itself is correlated between pairs. Therefore the Poisson error bars should be used only as a visual guide: they would underestimate the true uncertainties if used in a cosmological parameter analysis.

5.1.2 Monte Carlo method

We used a Monte Carlo method to compute the covariance matrix of $\xi_{++}(\theta)$ and $\xi_{\times\times}(\theta)$. The method is part theoretical and part empirical: it is based on a theoretical shear

power spectrum, but randomizes the real galaxies to correctly treat the noise properties of the survey. The advantages of the Monte Carlo method – as implemented here – are that spatially variable noise, intrinsic shape noise including correlations between the r and i band, and the survey window function are correctly represented. The principal disadvantages are that the cosmic shear field is treated as Gaussian and a particular cosmology must be assumed (see Eifler et al. 2009, for alternative approaches). However, so long as this cosmology is not too far from the correct one (an assumption that can itself be tested!), the Monte Carlo approach is likely to yield the best covariance matrix.

The Monte Carlo approach begins with the generation of a suite of 459 realizations of a cosmic shear field in harmonic space according to a theoretical spectrum. For our analysis, the theoretical spectrum was that from the *WMAP* 7-year (Larson et al. 2011) cosmological parameter set (flat ΛCDM; $\Omega_{\rm b}h^2 = 0.02258$; $\Omega_{\rm m}h^2 = 0.1334$; $n_{\rm s} = 0.963$; $H_0 = 71.0\,\mathrm{km\,s^{-1}\,Mpc^{-1}}$; and $\sigma_8 = 0.801$), and the shear power spectrum code used in Albrecht et al. (2009), itself based on the Eisenstein & Hu (1998) transfer function and the Smith et al. (2003) nonlinear mapping. The redshift distribution discussed in section 3.4.1, based on a calibration sample from DEEP2, VVDS, and PRIMUS, was used as the input to the shear power spectrum calculation.

From this power spectrum we generate a sample set of Gaussian E-mode shear harmonic space coefficients $a_{lm}^{\rm E}$. The full power spectrum is used at $l \leqslant 1500$; a smooth cutoff is applied from $1500 < l < 2000$ and no power at $l \geqslant 2000$ is included. This is appropriate for a covariance matrix since the power at smaller scales is shot noise dominated and cannot be recovered. (The E-mode power spectrum is $C_{1500}^{EE} = 3.6 \times 10^{-11}$, as compared to a shot noise of $\gamma_{\rm int}^2/\bar{n} \sim 1.8 \times 10^{-9}$.) No B-mode shear is included. The particle-mesh spherical harmonic transform code of Hirata et al. (2004a) with a 6144×3072 grid ($L' = 6144$) and a 400-node interpolation kernel ($K = 10$) was used to transform these coefficients into shear components (γ_1, γ_2) at the position $\hat{\boldsymbol{n}}_j$ of each galaxy j.[17]

---

[17] The use of a full-sky approach for the Monte Carlo realisations

A synthetic ellipticity catalogue was then generated as follows. For each galaxy, we generated a random position angle offset $\psi_j \in [0, \pi)$ and rotated the ellipticity in both r and i bands by ψ_j.[18] We then added the synthetic shear weighted by the shear responsivity to the randomised ellipticity to generate a synthetic ellipticity:

$$\boldsymbol{e}_j^{\mathrm{syn}} = \mathrm{e}^{2\mathrm{i}\psi_j} \boldsymbol{e}_j^{\mathrm{true}} + 1.73\boldsymbol{\gamma}(\hat{\boldsymbol{n}}_j). \qquad (26)$$

The 1.73 prefactor was estimated from Eq. (11), which we expected to be good enough for use in the Monte Carlo analysis, so that the Monte Carlos could be run in parallel with the shear calibration simulations. The latter gave a final result of 1.78 ± 0.04, which is not significantly different.

The direct pair-count correlation function code, in all versions (rr, ri, and ii) was run on each of the 459 Monte Carlo realisations, before combining the different correlations to get the weighted value via Eq. (21).

The Monte Carlo and Poisson error bars are compared in Fig. 12. The correlation coefficients of the correlation functions in different bins are plotted graphically in Fig. 13.

From each Monte Carlo correlation function we compute the COSEBIs via Eq. (23) and use their covariance matrix in our subsequent likelihood analysis. In order to test whether our covariance has converged, meaning that the number of realisations is sufficient to not alter cosmological constraints, we perform 3 likelihood analyses in σ_8 vs. Ω_m space varying the numbers of realisations from which we compute the covariance matrix (see Sec. 6 for detailed methodology; for now we are just establishing convergence of the covariance matrix). In Fig. 14 we show the 68 and 95 per cent likelihood contours, i.e. the contours enclose the corresponding fraction of the posterior probability (within the ranges of the parameters shown). We see that the contours hardly change when going from 300 to 400 realizations and show no change at all when going from 400 to 459 realisations, hence the 459 Monte Carlo realizations are sufficient for our likelihood analysis.

5.2 Systematic contributions to the covariance matrix

The following additional contributions are added to the Monte Carlo covariance matrix (and if appropriate the theory result) described in Sec. 5.1.2.

(i) The intrinsic alignment error was included following Sec. 3.2: the theory shear correlation function was reduced by a factor of 0.92, and an uncertainty of 4 per cent of the theory was added to the covariance matrix, i.e. we add an intrinsic alignment contribution

$$\mathrm{Cov}[\xi_i, \xi_j](\text{intrinsic alignment}) = 0.04^2 \xi_i^{\mathrm{(th)}} \xi_j^{\mathrm{(th)}}, \qquad (27)$$

where the theory curve (th) is obtained at the fiducial

---

[18] was not necessary for the SDSS Stripe 82 project, but was the simplest choice given legacy codes available to us.

[18] To simplify bookkeeping, the actual implementation was that a sequence of 10^7 random numbers was generated, and a galaxy was assigned one of these numbers based on its coordinates in a fine grid with 0.36 arcsec cells in (α, δ).
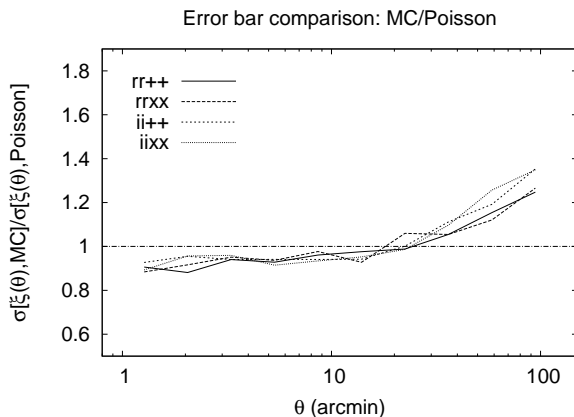
Figure 12. The ratio of error bars obtained by the Monte Carlo method to those obtained by the Poisson method, for 10 angular bins. The four curves show either rr or ii band correlation functions, and either the $++$ or $\times\times$ component. Note the rise in the error bars at large values of the angular separation, due to mode sampling variance.
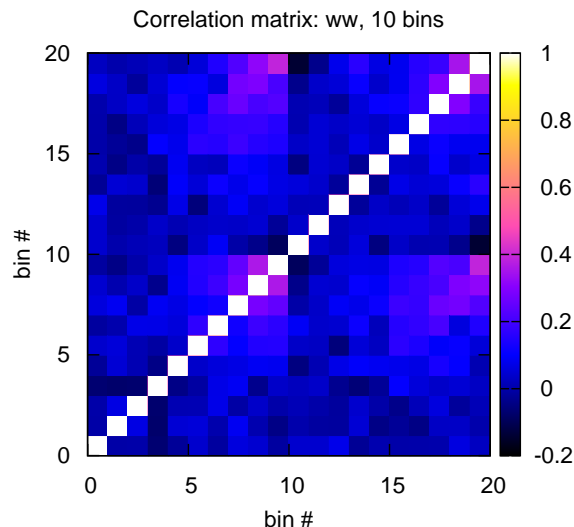
Figure 13. The matrix of correlation coefficients for the combined (ww) correlation functions in the 10 angular bins for which the correlation function is plotted in the companion figures. The bin number ranges from 0–9 for $\xi_{++}(\theta)$ and from 10–19 for $\xi_{\times\times}(\theta)$; all diagonal components are by definition equal to unity. Based on 459 Monte Carlo realisations.

WMAP7 point. This covariance matrix includes perfect correlation between radial bins, implying that we treat this systematic as being an effect with a fixed scaling with separation, so the only degree of freedom is its amplitude.

(ii) The stellar contamination was included following Sec. 3.5: the theory shear correlation function was reduced by a factor of 0.936, and an uncertainty of 3 per cent of the
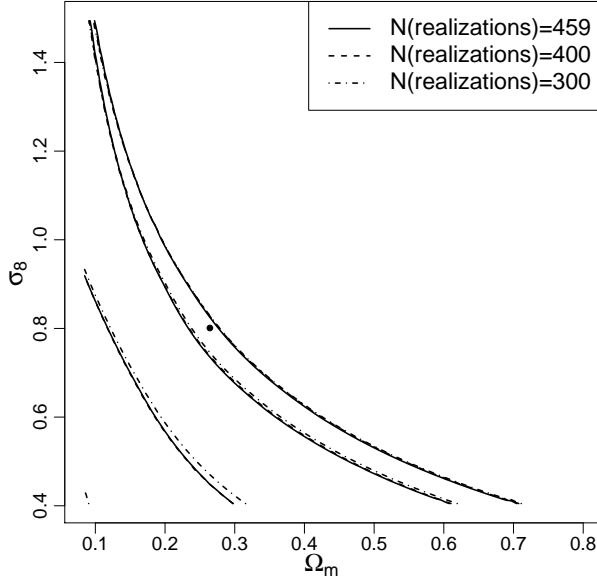
Figure 14. Convergence test of the σ_8 vs. Ω_m parameter constraints as a function of the number of Monte Carlo realizations used to compute the covariance. The plot shows the 68 and 95 per cent likelihood contours (however, the lower 95 per cent contours are not visible). The covariance includes statistical errors only.

theory was added to the covariance matrix, i.e. we add a stellar contamination contribution

$$\mathrm{Cov}[\xi_i, \xi_j](\text{stellar contamination}) = 0.03^2 \xi_i^{(\mathrm{th})} \xi_j^{(\mathrm{th})}, \qquad (28)$$

where the theory curve (th) is obtained at the fiducial WMAP7 point.

(iii) The implied error from the redshift distribution uncertainty is derived from 402 realisations of the sampling variance simulations as described in Sec. 3.4.2. We construct the covariance matrix of the predicted E-mode COSEBIs.

(iv) The shear calibration uncertainty was conservatively estimated in Sec. 3.3 to be ± 2.4 per cent, or equivalently 4.8 per cent in second-order statistics. We thus add another term to the covariance matrix,

$$\mathrm{Cov}[\xi_i, \xi_j](\text{shear calibration}) = 0.048^2 \xi_i^{(\mathrm{th})} \xi_j^{(\mathrm{th})}. \qquad (29)$$

(v) In Sec. 3.6, we described a procedure for including uncertainty due to additive PSF contamination. According to this procedure, the relevant systematics covariance matrix is related to the amplitude of the measured contamination signal:

$$\mathrm{Cov}[\xi_i, \xi_j](\text{PSF contamination}) = 0.9^2 \xi_{\mathrm{sg},i} \xi_{\mathrm{sg},j}, \qquad (30)$$

again assuming a fixed scaling with radius for this systematic uncertainty. Since all entries scale together, we do not spuriously "average down" our estimate of the systematic error by combining many bins.

The final data vector and its covariance matrix (including all the statistical and systematic components) are given in Tables A1 and A2. Note that given our procedure of applying the systematic corrections to the theory, the data vector is the observed one without any such corrections for the stellar contamination and intrinsic alignments contamination. With this in hand, we can estimate the significance

of the E- and B-mode signals described in section 4.3. The probability that the COSEBI E-mode signal that we observe is due to random chance given the null hypothesis (no cosmic shear) is 6.0×10^{-6}. The probability of measuring our B-mode signal due to random chance given the null hypothesis of zero B modes is .36, evidence that there is no significant B-mode power.

6   COSMOLOGICAL CONSTRAINTS

Having described the measured cosmic shear two-point statistics, and shown that the systematic bias in this measurement is small compared with the statistical constraints, we now turn to the cosmological interpretation. We work in the context of the flat ΛCDM parametrisation, taking where necessary the WMAP7 (Komatsu et al. 2011) constraints for our fiducial parameter values.

6.1   The prediction code: modeling second-order shear statistics

To produce a cosmological interpretation of our measured cosmic shear signal from our model framework, we require a method to convert a vector of cosmological parameters into a prediction of the observed cosmic shear signal. Due to projection effects, we expect that a significant fraction of the observed cosmic shear signal is produced by the clustering of matter on nonlinear scales, so a suitably accurate prediction algorithm must ultimately rely on numerical simulations of structure formation.

The prediction code used in our likelihood analysis is a modified version of the code described in Eifler (2011). We combine Halofit (Smith et al. 2003), an analytic approach to modeling nonlinear structure, with the Coyote Universe Emulator (Lawrence et al. 2010), which interpolates the results of a large suite of high-resolution cosmological simulations over a limited parameter space, to obtain the density power spectrum. The derivation is a two-step process: First, we calculate the linear power spectrum from an initial power law spectrum $P_\delta(k) \propto k^{n_\mathrm{s}}$ employing the dewiggled transfer function of Eisenstein & Hu (1998). The nonlinear evolution of the density field is incorporated using Halofit. In order to simulate wCDM models we follow the scheme implemented in ICOSMO (Refregier et al. 2011), interpolating between flat and open cosmological models to mimic Quintessence cosmologies (see Schrabback et al. 2010 for more details). In a second step, we match the Halofit power spectrum to the Coyote Universe emulator (version 1.1) power spectrum, which emulates P_δ over the range $0.002 \leqslant k \leqslant 3.4h/\mathrm{Mpc}$ within $0 \leqslant z \leqslant 1$ to an accuracy of 1 per cent. Wherever possible, the matched power spectrum exactly corresponds to the Coyote Universe Emulator; of course this is limited by the cosmological parameter space of the Emulator and its limited range in k and z. However, even outside the range of the Emulator, we rescale the Halofit power spectrum with a scale factor $P_\delta(\mathrm{Coyote})/P_\delta(\mathrm{Halofit})$ calculated at the closest point in parameter space (cosmological parameters, k, and z) where the Emulator gives results. Outside the range of the Emulator, the accuracy of this "Hybrid" density power spectrum is of course worse than 1 per cent, however it should be a significant improvement
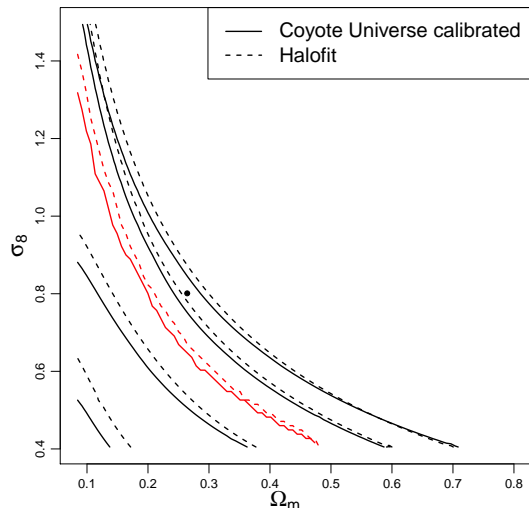
Figure 15. The 68 and 95 per cent likelihood contours of the combined data vector including a full treatment of systematics when using the Halofit prediction code (dashed) and when using the Coyote Universe-calibrated prediction code (solid). The red lines correspond to the best-fitting value of σ_8 for a given Ω_m. The dot indicates the WMAP7 best-fitting values.
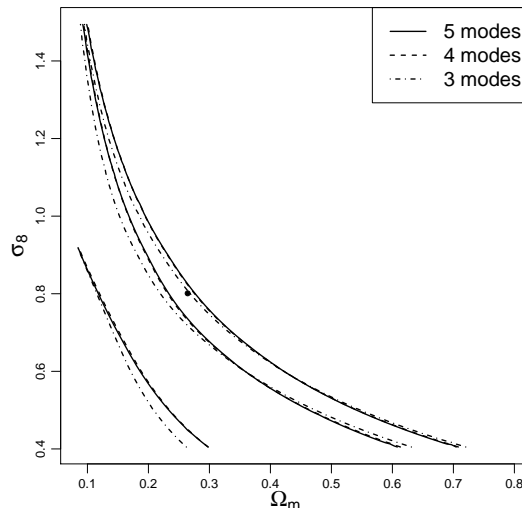

Figure 16. Convergence test of the σ_8 vs. Ω_m parameter constraints as a function of number of COSEBI modes in the data vector. The plot shows the likelihood contours enclosing 68 and 95 per cent of the posterior distribution. (The lower bounding curve for the 95 per cent contours is not visible on the plot.) The covariance contains statistical errors only. The dot indicates the WMAP7 best-fitting values.

over a density power spectrum from Halofit only. From the so-derived density power spectrum we calculate the shear power spectrum via Eq. (8) and the shear-shear correlation function via Eq. (7). As a final step, we transform these predicted correlation functions to the COSEBI basis as described above in Sec. 4.3.

For our final results in the (Ω_m, σ_8) likelihood analysis, we used both prediction codes; the results are compared in Fig. 15, where they are seen to agree to much better than 1σ. We therefore conclude that uncertainty in the theory predictions is sub-dominant to the other sources of systematic error, and to the statistical error.

6.2   Constructing the input data vector

For our primary science results, we use the measured 5 COSEBI modes (see Fig. 11, left panel). As a first step we want to determine the number of COSEBI modes that need to be included in our likelihood analysis. In Fig. 16 we show a likelihood analysis in the σ_8-Ω_m parameter space varying the number of modes in the data vector. We find that there is hardly a change in the likelihood contours when going from 4 to 5 modes; we therefore conclude that 5 modes is a sufficient number to capture the cosmological information encoded in our data set.

As shown in Eifler et al. (2008), the information content of the aperture mass dispersion can be greatly improved when including 1 data point of the shear-shear correlation function ξ_+ into the data vector; here we adopt this concept for the COSEBIs. The basic idea is that the data point of the correlation function is sensitive to scales of the power spectrum to which the COSEBIs are insensitive. We incorporate only a single data point of the correlation function as this is sufficient to capture the bulk of the additional information while simultaneously minimising possible B-mode contamination.

In order to determine the optimal scale of the data point that is to be included, we consider 10 bins of ξ_+ ranging from 1.3 to 97.5 arcmin and perform 10 likelihood analyses for a combined data vector consisting of 5 COSEBI modes and one additional data point of ξ_+. We quantify the information content through the so-called q figure of merit (q-FoM)

$$q = \sqrt{|\mathbf{Q}|}, \quad \text{where}$$
$$Q_{ij} = \int \mathrm{d}^2\boldsymbol{\pi} \, p(\boldsymbol{\pi}|\mathbf{d}) \, (\pi_i - \pi_i^{\mathrm{f}})(\pi_j - \pi_j^{\mathrm{f}}), \quad (31)$$

$\boldsymbol{\pi} = (\Omega_m, \sigma_8)$ is the parameter vector, $p(\boldsymbol{\pi}|\mathbf{d})$ is the posterior likelihood at this parameter point, and π_i^{f} denotes the fiducial parameter values. If the likelihood in parameter space (i.e. the posterior probability) is Gaussian, the q-FoM corresponds to the more common Fisher matrix based figure of merit $f = 1/|\sqrt{\mathbf{F}}|$. The Fisher matrix $\mathbf{F}$ can be interpreted as the expectation value of the inverse parameter covariance evaluated at the maximum likelihood estimate parameter set, which in our ansatz corresponds to the fiducial parameters. Mathematically we can express this equivalence as

$$f = \frac{1}{\sqrt{|\mathbf{F}|}} = \sqrt{|\mathbf{C}_\pi|} = \sqrt{|\mathbf{Q}|} = q. \quad (32)$$

Since the assumption of a Gaussian posterior is clearly violated in the σ_8-Ω_m parameter space, we perform a full likelihood analysis and calculate q to quantify the size of the likelihood. Note that smaller q-FoM is "better."

We varied the angular scale (in arcmin) of the added $\xi_+(\theta)$ data point, and found a minimal q-FoM at $\theta = 37.8$ arcmin. We will use this scale for the additional ξ_+ data point henceforth. Note that this analysis uses a simulated input data vector in order to avoid biases from designing a statistical test based on the observed data. The constraints coming from the various possible data vectors – the COSEBIs, the COSEBIs supplemented with a single ξ_+ point, and
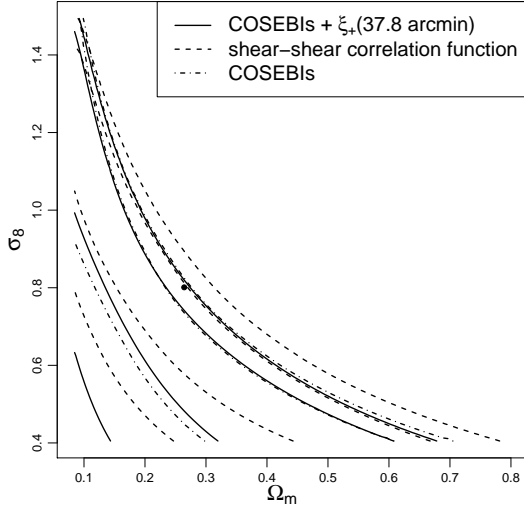
Figure 17. The likelihood contours of the combined data vector (solid), the shear-shear correlation function (dashed), and the COSEBIs (dotted) data vector to illustrate how much information is gained when including the additional data point. Note that the COSEBIs' lower 95 per cent contour is outside the considered region. The dot indicates the WMAP7 best-fitting values.
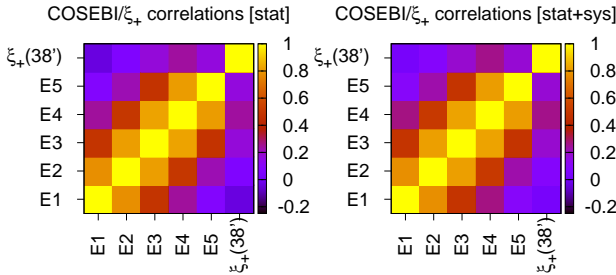
Figure 18. The correlation matrix of the COSEBI modes 1–5 ("E1...E5" in the figure) and $\xi_+(38')$. The left panel shows only the statistical (Monte Carlo) errors, and the right panel includes the systematics as well.

the full shear correlation function – are compared in Fig. 17. They are not identical, which is expected since they weight the data in different ways, but are consistent with each other.

The COSEBI modes are highly correlated with each other, and they are correlated to a lesser extent with ξ_+ at 38 arcmin. The correlation matrix is shown in Fig. 18, and the corresponding covariance matrix is tabulated in the Appendix in Table A2.

6.3 Parameter Fits

We perform all of our fits to a standard five-parameter ΛCDM model[19]. For the initial likelihood analysis, we fix n_s, $\Omega_b h^2$, $\Omega_m h^2$, and w_0 at their fiducial best-fit WMAP7 values (Komatsu et al. 2011), and vary σ_8. The upper panel of

---

[19] The optical depth to reionization τ is a sixth parameter implicitly included in the WMAP7 chains, but with no effect on the lensing shear correlation function.

Fig. 19 shows the likelihood of σ_8 with all other parameters fixed, with a value at the peak and 68 per cent confidence interval of $0.636^{+0.109}_{-0.154}$. For a survey of this size and depth, the constraints are comparable to the statistically achievable confidence limits.

We also perform a likelihood analysis fixing three parameters, and varying Ω_m and σ_8 simultaneously, as these two parameters are much more sensitive to the measured cosmic shear signal than the others. The resulting two-dimensional constraints are shown in the bottom panel of Fig. 19. Our 68 per cent confidence limits on the degenerate product $\sigma_8 \left(\frac{\Omega_m}{0.264}\right)^{0.67}$ are $0.65^{+0.12}_{-0.15}$ for the Coyote Universe prediction code (see Fig. 19, solid red line), and $\sigma_8 \left(\frac{\Omega_m}{0.264}\right)^{0.72} = 0.67^{+0.12}_{-0.15}$ for the Halofit prediction code (see Fig. 19, dashed red line).

We show the effects of removing each systematic error correction, Fig. 19 also shows, for both the one- and two-dimensional analyses, the impact of systematic error corrections. The combined effects of these uncertainties are clearly substantially smaller than the statistical error on the amplitude of the shear signal.

Finally, we adopt the WMAP7 likelihoods as priors, and evaluate our likelihood at each link in the WMAP7 Markov chain. For each chain element, we assign a weight equal to our likelihood function evaluated at the parameter vector for that chain element. For each of the parameter constraint plots shown here, we first assign each Markov Chain Monte Carlo (MCMC) chain element to a point on a regular grid in the parameter space; the value of the marginalised likelihood at each grid-point, $H_{i,j}$ is then the sum of our likelihood weights over the MCMC chain elements at the (i, j) grid-point,

$$H_{i,j} = \sum_k I_k(i,j) L_k, \qquad (33)$$

where the indicator function $I_k(i,j)$ is equal to unity when the (i, j) grid-point in parameter space is nearest the kth chain element, and zero otherwise. The likelihood L_k for each chain element is evaluated in the usual way as:

$$L_k = \exp\left(-\frac{\bar{\boldsymbol{d}}_k^T \mathbf{C}^{-1} \bar{\boldsymbol{d}}_k}{2}\right). \qquad (34)$$

Here $\mathbf{C}$ is the full covariance matrix for the measurement, incorporating both the statistical and systematic uncertainties, and the normalization is arbitrary. The data vector $\bar{\boldsymbol{d}}_k$ is the extended COSEBI vector described above; where shown, the WMAP7 priors are simply this sum with $L_k = 1$ for each point.

We estimate the detection significance for the final signal, the difference $\sqrt{-2\Delta \log L}$ between the highest-likelihood Markov Chain element for both the ΛCDM and wCDM models and the likelihood evaluated with no signal. The 1σ detection significances for these two models are 2.64 and 2.88, respectively. This is not the significance of the detection of cosmic shear (as in Sec. 5.2), but rather a measurement of the likelihood of these two models given the combination of WMAP7 priors with this experiment.

In Fig. 20, we show marginalized posterior likelihoods in the case of fixed ΛCDM (i.e., $w = -1$) for $\Omega_m h^2$, $\Omega_b h^2$, n_s, and σ_8. The results with a free equation of state of dark energy (wCDM) are in Fig. 21. Our measurement provides
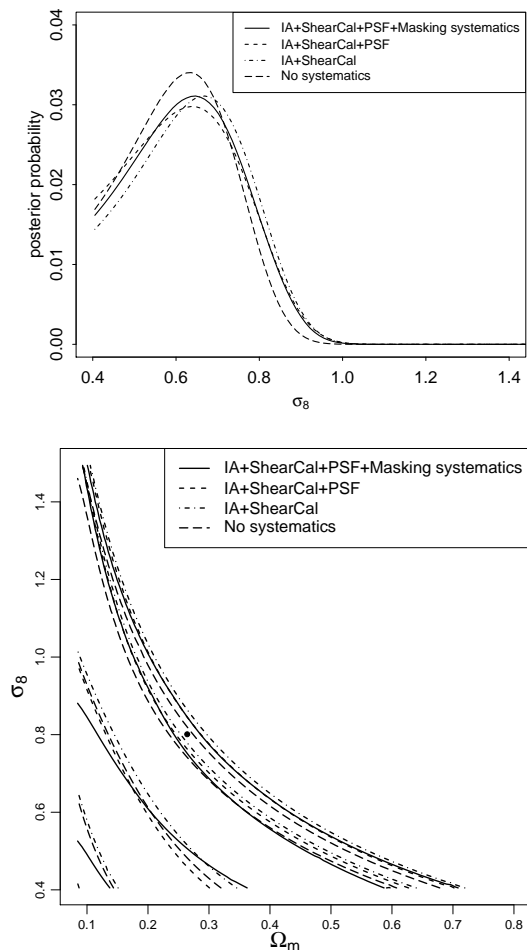
Figure 19. The effect of systematic errors in the 1-D likelihood of σ_8 (upper panel) and in the 2-D constraints (68 per cent likelihood contours only) in the $\sigma_8 - \Omega_m$ plane (lower panel). The solid curve shows our final analysis, while the other curves show results including subsets of the systematic errors. The dot-dashed curve labeled "no systematics" shows only the statistical errors, without any systematic error corrections either to the theory or to the covariance matrix. The dot indicates the WMAP7 best-fitting values.

some additional constraints beyond those from WMAP7 on these parameters. In particular, the low amplitude of the measured shear signal rules out some of the previously allowed volume of $\Omega_m h^2$ and σ_8 WMAP7 constraints.

7 CONCLUSIONS

Using coadded imaging constructed from SDSS Stripe 82 data, we constructed a weak lensing catalogue of 1 328 885 galaxies covering 168 square degrees (Paper I), and showed that the additive shear systematics arising from the PSF are negligible compared to the cosmic shear signal. In this paper, we carried out a cosmic shear measurement that resulted in a 20 per cent constraint on σ_8 (with all other cosmological parameters fixed). This adds constraining power beyond that from WMAP7, and serves as an important independent data point on the amplitude of the matter power spectrum at late times. In particular, the primary

CMB anisotropies presently provide only a modest constraint on $\Omega_m h^2$, and (due to the effect of matter density on the growth of structure) there is then an elongated allowed region in the $(\Omega_m h^2, \sigma_8)$ plane; see Fig. 20. The WMAP7-allowed region is ideally oriented for lensing to play a role: the lensing signal at the high-$\Omega_m h^2$, high-σ_8 end of the ellipse leads to a much higher lensing signal than low $\Omega_m h^2$, low σ_8. The low amplitude of cosmic shear observed in this paper eliminates the high-$\Omega_m h^2$, high-σ_8 solutions, and leads to a WMAP7+SDSS lensing solution of $\sigma_8 = 0.784^{+0.028}_{-0.026}(1\sigma)^{+0.055}_{-0.054}(2\sigma)$ and $\Omega_m h^2 = 0.1303^{+0.0047}_{-0.0048}(1\sigma)^{+0.0091}_{-0.0092}(2\sigma)$; the 2σ error ranges are respectively 14 and 17 per cent smaller than for WMAP7 alone.

We have also carefully evaluated other sources of uncertainty such as the source redshift distribution, intrinsic alignments, and shear calibration, to ensure that our measurement is dominated by statistical errors rather than systematic errors. This achievement is important when considering that (i) the SDSS data were never designed with this application in mind, and indeed includes several features (e.g. the minimal amount of cross-scan dithering) that cause significant difficulty, and (ii) with the multitude of upcoming multi-exposure lensing surveys in the next few years, it is important to cultivate new data analysis techniques (such as the one used here) that are capable of producing homogeneous data with tight control over PSF anisotropies. As a quantitative measure of the extent of PSF correction possible with SDSS data, we take the RMS residual spurious shear at a particular scale estimated from the star-galaxy correlations,

$$\gamma_{\rm rms,eq}(\theta) = \frac{\sqrt{\mathcal{R}_{\rm psf}\, \xi_{+,\rm sg}(\theta)}}{\mathcal{R}}. \tag{35}$$

From Fig. 6, we see that this is $\sim 2 \times 10^{-3}$ at the smallest scales (1–6 arcmin), is $< 10^{-3}$ at scales $\theta > 0.1$ degree, and drops to 3.7×10^{-4} in the final bin (1.2–2.0 degrees).[20] There is almost no difference between the $++$ and $\times\times$ signals, suggesting that the spurious additive ellipticity signal contains similar amounts of E- and B-modes[21]; something similar was seen in the SDSS single-epoch data via run-by-run comparisons of ellipticity measurements on the same galaxies (Mandelbaum et al. 2006b, Fig. 8). This is good news for the use of the B-mode as a diagnostic of PSF systematics, although an understanding of the generality of this pattern remains elusive.

A major lesson learned from this project is the importance of *masking bias*, in which the intrinsic orientation of a galaxy affects whether it falls within the survey mask. This is likely the main reason why we had to implement the $\langle e_1 \rangle$ projection. While we have clearly not exhausted the range of options for removing this bias at the catalogue level, future surveys should be designed to produce more uniform data quality via an appropriate dithering strategy and suppress the masking bias at the earliest stages of the analysis.

Our major limitation in the end was the source number density, which was driven by the fact that our PSF-matching procedure was limited by the worst seeing in the images that

---

[20] We used $\mathcal{R}_{\rm psf} = 0.9$ and $\mathcal{R} = 1.776$, as described in the text.
[21] Recall that $\xi_{++}(\theta) - \xi_{\times\times}(\theta)$ and $P_E(\ell) - P_B(\ell)$ are J_4 Hankel transforms of each other.
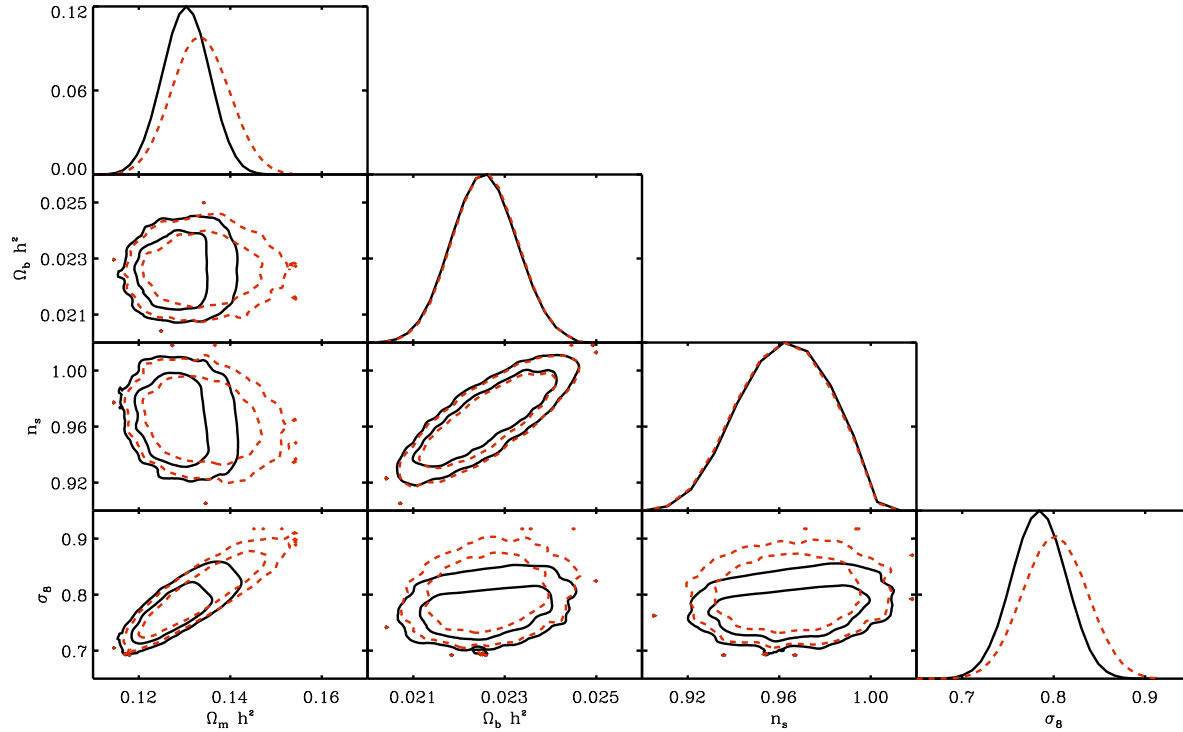
Figure 20. The cosmological parameter constraints using the extended COSEBI data vector, fixing the dark energy equation of state w at -1, but allowing all other parameters to vary. Off-diagonal panels show joint two-dimensional constraints after marginalization over all the other parameters, which are shown. For these, the red contours show the WMAP7 priors containing 68.5 and 95.4 per cent of the posterior probability. The black contours are the same but for WMAP7+SDSS lensing. Diagonal panels show the fully-marginalized one-dimensional posterior distribution for each parameter; for these panels, the red (dashed) contours show the marginalized WMAP7 constraints.

we use, and therefore we had to eliminate the images with seeing worse than the median. This means that the coadds were not as deep as they could have been, and the final effective seeing was 1.31 arcsec (full-width half maximum). In principle this will be an obstacle to applying this technique in the future, but in fact, that statement depends on context. For example, for a survey such as HSC or LSST where we expect typically ~ 0.7 arcsec seeing, and with plans to preferentially use the best-seeing nights for r and i-band imaging that will be used for shape measurement, it is conceivable that nearly all images intended for lensing will have seeing in the 0.6–0.8 arcsec range. In that context, a PSF-matched coadd that has the rounding kernel applied may actually not result in much loss of information about the shapes of most useful galaxies, and will have the advantage of the removal of PSF anisotropies. Moreover, even for surveys for which the loss of information that results from this method may not be suitable for the final cosmological analysis, this method may still serve as a useful diagnostic of the additive PSF systematics.

Figure 21. The cosmological parameter constraints using the extended COSEBI data vector, varying all five parameters. Off-diagonal panels show joint two-dimensional constraints after marginalization over all the other parameters, which are shown. For these, the red contours show the WMAP7 priors containing 68.5 and 95.4 per cent of the posterior probability. The black contours are the same but for WMAP7+SDSS lensing. Diagonal panels show the fully-marginalized one-dimensional posterior distribution for each parameter; for these panels, the red (dashed) contours show the marginalized WMAP7 constraints.

REFERENCES

Albrecht A. et al., 2006, preprint, astro-ph/0609591
Albrecht A. et al., 2009, preprint, arXiv:0901.0721
Bacon D. J., Refregier A. R., Ellis R. S., 2000, MNRAS, 318, 625
Benabed K., van Waerbeke L., 2004, PRD, 70, 123515
Benjamin J. et al. 2007, MNRAS, 381, 702
Bernstein G. M., Jarvis M., 2002, AJ, 123, 583
Bernstein G., Huterer D., 2010, MNRAS, 401, 1399
Bernstein G., 2010, MNRAS, 406, 2793
Blazek J., McQuinn M., Seljak U., 2011, JCAP, 5, 10
Catelan P., Kamionkowski M., Blandford R., 2001, MNRAS, 320, L7
Coil A. L. et al. 2011, ApJ, 741, 8
Crittenden R. G., Natarajan P., Pen U.-L., Theuns T., 2001, ApJ, 559, 552
Crittenden R. G., Natarajan P., Pen U.-L., Theuns T., 2002, ApJ, 568, 20
Croft R., Metzler C., 2000, ApJ, 545, 561
Cunha C. E., Lima M., Oyaizu H., Frieman J., Lin H., 2009, MNRAS, 396, 2379

Davis M., et al. 2003, in P. Guhathakurta ed., Proc. SPIE Vol. 4834, Discoveries and Research Prospects from 6- and 10-Meter-Class Telescopes II. SPIE, Bellingham, p. 161

Eifler T., Kilbinger M., Schneider P., 2008, A&A, 482, 9

Eifler T., Schneider P., Hartlap J., 2009, A&A, 502, 721

Eifler T., Schneider P., Krause E., 2010, A&A, 510, 7

Eifler T., 2011, MNRAS, 418, 536

Eisenstein D., Hu W., 1998, ApJ, 496, 605

Fu L. et al., 2008, A&A, 479, 9

Fu L., Kilbinger M., 2010, MNRAS, 401, 1264

Heavens A., Refregier A., Heymans C., 2000, MNRAS, 319, 649

Heymans C., Rowe B., Hoekstra H., Miller L., Erben T., Kitching T., Van Waerbeke L., 2011, preprint (arXiv:1110.4913)

Hilbert S., Hartlap J., White S. D. M., Schneider P., A&A, 499, 31

Hirata C., Seljak U., 2003, MNRAS, 343, 459

Hirata C., Padmanabhan N., Seljak U., Schlegel D., Brinkmann J., 2004a, PRD, 70, 103501

Hirata C. M. et al., 2004b, MNRAS, 353, 529

Hirata C. M., Seljak U., 2004, PRD, 70, 63526

Hirata C. M., Mandelbaum R., Ishak M., Seljak U., Nichol R., Pimbblet K. A., Ross N. P., Wake D., 2007, MNRAS, 381, 1197

Hoekstra H. et al. 2006, ApJ, 647, 116

Hopkins P., Bahcall N., Bode P., 2005, ApJ, 618, 1

Huff E. M., Hirata C. M., Mandelbaum R., Schlegel D., Seljak U., Lupton R. H., 2011, preprint (arXiv:1111.6958), "Paper I"

Huterer D., 2002, PRD, 65, 63001

Ilbert O. et al., 2009, ApJ, 690, 1236

Jain B., Seljak U., White S., 2000, ApJ, 530, 547

Jing Y., 2002, MNRAS, 335, L89

Joachimi B., Mandelbaum R., Abdalla F. B., Bridle S. L., 2011, A&A, 527, 26

Jouvel S. et al., 2009, A&A, 504, 359

Kaiser N., 2000, ApJ, 537, 555

Kaiser E., Wilson G., Luppino G. A., 2000, preprint (astro-ph/0003338)

Kaiser N., Burgett W., Chambers K., Denneau L., Heasley J., Jedicke R., Magnier E., Morgan J., Onaka P., Tonry J., 2010, in Society of Photo-Optical Instrumentation Engineers (SPIE) Conference Series, Vol. 7733, 12

Kilbinger M., Schneider P., Eifler T., 2006, A&A, 457, 15

Koekemoer A., Fruchter A., Hook R., Hack W., 2002, The 2002 HST Calibration Workshop: Hubble after the Installation of the ACS and the NICMOS Cooling System, eds. Arribas, Koekemoer, & Whitmore, p. 337

Koekemoer A. et al., 2007, ApJS, 172, 196

Komatsu E. et al., 2011, ApJS, 192, 18

Kovač K. et al., 2010, ApJ, 708, 505

Krause E., Hirata C. M., 2010, A&A, 523, 28

Kristian J., 1967, 147, 864

Kristian J., Sachs R. K., 1966, ApJ, 143, 379

Larson D. et al., 2011, ApJS, 192, 16

Laszlo I., Bean R., Kirk D., Bridle S., 2011, preprint, arXiv:1109.4535

Lawrence E., Heitmann K., White M., Higdon D., Wagner C., Habib S., Williams B., 2010, ApJ, 713, 1322

Leauthaud A. et al., 2007, ApJS, 172, 219

Le Fèvre O., et al. 2005, A&A, 439, 845

Lima M., Cunha C. E., Oyaizu H., Frieman J., Lin H., Sheldon E. S., 2008, MNRAS, 390, 118

LSST Science Collaborations et al. 2009, preprint (arXiv:0912.0201)

Ma Z., Bernstein G., 2008, ApJ, 682, 39

Ma Z., Hu W., Huterer D., 2006, ApJ, 636, 21

Madgwick D. S., et al. 2003, ApJ, 599, 997

Mandelbaum R., Hirata C. M., Seljak U., Guzik J., Padmanabhan N., Blake C., Blanton M. R., Lupton R., Brinkmann J., 2005, MNRAS, 361, 1287

Mandelbaum R., Hirata C. M., Ishak M., Seljak U., Brinkmann J., 2006a, MNRAS, 367, 611

Mandelbaum R., Hirata C. M., Broderick T., Seljak U., Brinkmann J., 2006b, MNRAS, 370, 1008

Mandelbaum R., Hirata C. M., Leauthaud A., Massey R. J., Rhodes J., 2011a, preprint (arXiv:1107.4629)

Mandelbaum R. et al. 2011b, MNRAS, 410, 844

Massey R. et al., 2007a, ApJS, 172, 239

Massey R., Rowe B., Refregier A., Bacon D., Bergé J., 2007b, MNRAS, 380, 229

Massey R., Stoughton C., Leauthaud A., Rhodes J., Koekemoer A., Ellis R., Shaghoulian E., 2010, MNRAS, 401, 371

Miyazaki S., Komiyama Y., Nakaya H., Doi Y., Furusawa H., Gillingham P., Kamata Y., Takeshi K., Nariai K., 2006, in Society of Photo-Optical Instrumentation Engineers (SPIE) Conference Series, Vol. 6269, 9

Moster B., Somerville R., Newman J., Rix H.-W., 2011, ApJ, 731, 113

Nakajima R., Mandelbaum R., Seljak U., Cohn J. D., Reyes R., Cool R., 2011, preprint (arXiv:1107.1395)

Okumura T., Jing Y. P., Li C., 2009, ApJ, 694, 214

Perlmutter S. et al., 1999, ApJ, 517, 565

Refregier A., 2003, MNRAS, 338, 35

Refregier A., Amara A., Kitching T. D., Rassat, A., 2011, A&A, 528, 33

Reyes R., Mandelbaum R., Gunn J. E., Nakajima R., Seljak U., Hirata C. M., 2011, preprint (arXiv:1110.4107)

Rhodes J. et al., 2007, ApJS, 172, 203

Riess A. G. et al., 1998, AJ, 116, 1009

Schmidt F., Rozo E., Dodelson S., Hui L., Sheldon E., 2009, ApJ, 702, 593

Schneider P. et al. 2002, A&A, 389, 729

Schneider P., Kilbinger M., 2007, A&A, 462, 841

Schneider P., Eifler T., Krause E., 2010, A&A, 520, 116

Schrabback T. et al. 2010, A&A, 516, 63

Scoville N. et al., 2007a, ApJS, 172, 1

Scoville N. et al., 2007b, ApJS, 172, 38

Semboloni E. et al. 2006, A&A, 452, 51

Sheldon E., Cunha C., Mandelbaum R., Brinkmann J., Weaver B., 2011, preprint (arXiv:1109.5192)

Smith R. et al., 2003, MNRAS, 341, 1311

The Dark Energy Survey Collaboration 2005, preprint (astro.ph/05010346)

van Waerbeke L. et al., 2000, A&A, 358, 30

van Waerbeke L., White M., Hoekstra H., Heymans C., 2006, Astropart. Phys., 26, 91

Wechsler R., 2004, in 'Clusters of Galaxies: Probes of Cosmological Structure and Galaxy Evolution,' Eds. Mulchaey J. S., Dressler A., Oemler A., Pasadena, 53

Wittman D. M., Tyson J. A., Kirkman D., Dell'Antonio I., Bernstein G., 2003, MNRAS, 341, 1311

Zhang J., 2011, MNRAS, 414, 1047

Table A1. Our data vector. The first five elements are COSEBI mode amplitudes; the final is the correlation function averaged in the range $29.2296 \leqslant \theta \leqslant 44.9730$.

4.89797E-10
1.28335E-09
1.25136E-09
1.45616E-09
8.92333E-10
1.46457E-05

Table A2. The covariance matrix for the data vector shown in table A1.

Data vector index	Data vector index	Covariance
0	0	3.37161E-20
0	1	4.67637E-20
0	2	4.00484E-20
0	3	2.49916E-20
0	4	9.84257E-21
0	5	3.01770E-17
1	1	1.06383E-19
1	2	1.19226E-19
1	3	8.39508E-20
1	4	3.86519E-20
1	5	1.82344E-16
2	2	1.99923E-19
2	3	1.87469E-19
2	4	1.12196E-19
2	5	5.07790E-16
3	3	2.56568E-19
3	4	2.13363E-19
3	5	8.02118E-16
4	4	2.67774E-19
4	5	5.67797E-16
5	5	3.68112E-11

APPENDIX A: THE DATA VECTOR AND COVARIANCE MATRIX.

Here we reprint the data vector and covariance matrix used in this measurement. The code used to project the correlation function onto the COSEBI basis functions is available from the authors upon request.